Sex dependent effects of amyloidosis on functional network 'hub' topology is associated with downregulated neuronal gene signatures in the APP*swe*/PSEN1dE9 double transgenic mouse

Zachary D. Simon[1,2], Karen N. McFarland[3,5], Todd E. Golde[5], Paramita Chakrabarty[2,4], Marcelo Febo[1,2]

1) Department of Psychiatry, University of Florida, Gainesville, FL, USA

2) Department of Neuroscience, University of Florida, Gainesville, FL, USA

3) Department of Neurology, University of Florida, Gainesville, FL, USA

4) Center for Translational Research in Neurodegenerative Disease, University of Florida, Gainesville, FL, USA

5) Department of Pharmacology and Chemical Biology; Center for Neurodegenerative Disease, Emory University, Atlanta, GA, USA

Short title: Sex dependent effects of amyloidosis

Address correspondence to:

Marcelo Febo, PhD,

Email: febo@ufl.edu,

Phone: 352-294-4911

Address: Department of Psychiatry, University of Florida, 1149 S. Newell Dr., Bldg. 059, Room L4-100F, Gainesville, Florida 32611, USA

Highlights

- Amyloidosis was associated with increased functional connectivity in a dorsal striatal/amygdala network, an effect paralleled by increased differentially expressed genes involved in the immune response.
- Amyloidosis increased eigenvector centrality, a network measure reportedly altered in Alzheimer's disease, but this effect was only observed in female mice.
- In female mice, amyloidosis downregulated a cluster of differentially expressed genes known to play roles in GABAergic and dopaminergic signaling, anxiogenic responses and motor activity.

Abstract

Extracellular beta-amyloid (Aβ) is thought to cause impairments in brain wide functional connectivity, although mechanisms linking Aβ to broader functional network processing remain elusive. In the present study, we evaluated the effects of Aβ on fear memory and functional connectome measures in male and female mice. Middle-aged (9-11mo) double transgenic APP-PS1 mice and age and sex-matched controls were tested on a fear conditioning protocol and then imaged at 11.1 Tesla. Brains were harvested and processed for analysis of Aβ plaques and Iba1 immunolabeling in neocortical areas, hippocampus, and basolateral amygdala. Additional RNA sequencing data from separate age, strain, and sex matched mice were analyzed for differentially expressed genes (DEGs) and weighted gene co-expression networks. In both male and female mice, we observed increased functional connectivity in a dorsal striatal/amygdala network as a result of Aβ. Increased functional connectivity within this network was matched by increases in APP gene expression, Aβ and Iba1 immunolabeling, and an upregulated cluster of DEGs involved in the immune response. Conversely, the network measure representing node 'hubness', eigenvector centrality, was increased in prefrontal cortical brain regions, but only in female APP-PS1 mice. This female specific-effect of amyloid was associated with downregulation of a cluster of DEGs involved in cortical and striatal GABA transmission, anxiogenic responses, and motor activity, in female APP-PS1 mice, but not males. Our results contribute to a growing literature linking between Aβ, immune activation and functional network connectivity. Furthermore, our results reveal effects of Aβ on gene expression patterns in female mice that may contribute to amyloidosis-induced dysregulation of non-cognitive circuitry.

Keywords: Amyloid, sex, gene networks, functional connectivity networks, fear memory

1. Introduction

Early onset Alzheimer's disease (AD) has an estimated prevalence of 1-5%, with the remaining 95% of all cases representing late onset sporadic forms (Alzheimer's Association, 2022). Approximately 200,000 individuals in the US suffer symptoms as early as 30-40 years of age, compared to non-familial AD which emerges at or after 65 (Hendriks et al., 2021). Studies of isolated familial cases have led to the discovery of several heritable amyloid precursor protein (APP) mutations and over 200 highly penetrant mutations in presenilin1 (PSEN1) that are causative for a percentage of early onset cases (D'Argenio and Sarnataro, 2020; Guerreiro et al., 2012). Familial AD involves mutation-specified amino acid substitutions in N- or C-terminal domain residues or Aβ regions of APP that cause aberrant APP processing, increase beta-amyloid (Aβ) levels and aggregation and extracellular Aβ plaque formation (D'Argenio and Sarnataro, 2020). The Swedish APP (APP*swe*) mutations, for example, produces amino acid substitutions (K670N, M671L) near the beta-secretase cleavage site of APP, leading to increased production of a 42 amino acid long Aβ peptide (Aβ42) (Guerreiro et al., 2012). Deletion of exon-9 in the PSEN1 gene sequence impairs gamma-secretase activity, which results in formation of aggregation prone Aβ42 (Guerreiro et al., 2012). Aβ is thought to mediate functional deficits in neurotransmission, including changes adversely impacting the activity of both excitatory and inhibitory neurons (Fuhrer et al., 2017; Mitew et al., 2013). Understanding these and other Aβ-linked functional changes, at the genetic, neuronal and neural circuit scales, is fundamental to uncovering targetable early pathology and neural signatures driving behavioral and cognitive changes in early onset and sporadic forms of AD.

Many reports on changes in excitatory and inhibitory neurons and synapses in AD brains are extrapolated from postmortem assessments (Dominguez-Alvaro et al., 2018; Fuhrer et al., 2017; Garcia-Marin et al., 2009; Kurucu et al., 2022). These neuronal changes, and their broader effects on network activity in AD, has been further explored in mice harboring human familial APP mutations (Niraula et al., 2024; Verret et al., 2012) and resting state functional magnetic resonance imaging studies (fMRI) (Buckner et al., 2009). Functional neuroimaging studies of early onset AD have reported widespread functional connectivity declines across multiple well establish networks (Adriaanse et al., 2014), particularly in default mode network (DMN) regions (Canu et al., 2017). This includes lower connectome measures of network strength, efficiency and clustering in frontoinsular, parietal, temporal and occipital cortices (Filippi et al., 2017), and reduced eigenvector centrality in bilateral medial temporal gyrus, right posterior hippocampal gyrus, and right postcentral gyrus (Zhou et al., 2021). Interestingly, there is some disagreement

between studies in terms of the specific regions affected and extent of reductions in functional connectivity and connectome measures. Pini *et al* reported a greater reduction in hippocampal connectivity to a group of cortical memory related regions in late onset versus early onset AD (Pini et al., 2020). Adriaanse *et al* observed broad functional connectivity declines in early onset AD compared to late onset, the latter mostly had reductions in the DMN compared to controls (Adriaanse et al., 2014). Yet, others have reported only DMN reductions relative to controls in early onset AD (Canu et al., 2017). All of the above studies use similarly aged subjects, around the age of 60 and matched control groups. Although pathology of AD is highly characterized by amyloidogenic mechanisms related to APP and PSEN mutations, there are other disease contributing genes differentially expressed in this population (Cacace et al., 2016; Cochran et al., 2019). Moreover, there are significant sex differences in the genetic architecture conferring resilience to AD, particularly cognitive resilience (Eissman et al., 2022). How this translates to functional brain changes in males versus females in response to AD pathologies remains an area of active research. Thus, the oligogenic contributions to AD, and important biological factors such as sex, warrant consideration in experiments to examine mechanistic links between Aβ and brain functional connectivity.

Functional neuroimaging studies in transgenic rodents harboring APP, PSEN1 and other AD causative or moderate-to-high risk mutations, selectively or in combination, can help clarify specific gene-pathology-brain functional connectivity interactions. A number of animal fMRI studies have begun to address Aβ-functional connectivity interactions, and these shown results consistent with some human studies of early onset AD (Grandjean et al., 2016; Grandjean et al., 2014b; Parent et al., 2017; Shah et al., 2013). Mouse fMRI studies have revealed nuanced interactions between Aβ aggregation and functional connectivity outcomes (Grandjean et al., 2016), which calls for attention to how APP is processed and how it interacts with other AD genes. Here we report new findings in the APP-PS1 mouse (Jankowsky et al., 2004) to expand on the existing literature on the relationship between Aβ and functional connectome changes. Further, we report a potentially important link between female-specific effects of Aβ on functional connectome node eigenvector centrality and brain gene expression. The differentially expressed genes specifically affected by Aβ in females include several genes in involved in striatal inhibitory gamma amino butyric acid (GABA) transmission.

2. Materials and Methods

2.1 Subjects and Data

Mice were housed in age- and sex-matched groups of 3-4 in a temperature- and humidity-controlled room, inside conventional air filtered cages (dimensions: 29 x 18 x 13 cm) with food and water available *ad libitum* (vivarium lights on from 07:00-19:00 hours). Transgenic (TG) cohorts were generated in house by breeding heterozygous male mice bearing amyloid precursor protein (APP) with the Swedish familial mutation and exon 9 deficient presenilin-1 (PSEN1) and hybrid C57BL6/J/6xC3H F1 females (Envigo)(Jankowsky et al., 2004). APP-PS1 mice develop gliosis and plaque accumulation starting at 6mo and cognitive and behavioral impairments as early as 8 mo (Janus et al., 2015). Control mice (NTG) were littermate non-transgenic mice and all groups contained male and female mice. Experiments started when mice were 10-11 months of age(mo), which corresponds to high amyloidosis, gliosis, with previously reported impairments in cognitive function and other non-cognitive behaviors (Janus et al., 2015). The behavior and imaging experiment group sizes were 13 NTG controls (including 4 female NTG) and 15 TG mice (including 7 female TG). The tissue histology group sizes differed between regions based on slice quality. Groups were 8-9 NTG controls (including 3-4 female NTG) and 11-13 TG mice (including female 5-7 TG). Forebrain RNA sequence data of the APP/PS1 mice were obtained from the AD Knowledge Portal synapse.org repository (Project SynID: syn2580853, title: “The Tau and APP Mouse Model (TAUAPPms) Study”). The dataset included 9-12 mo NTG (n=15, including 7 NTG females) and 12 mo TG mice (n=11, including 5 TG females). All procedures received prior approval from the Institutional Animal Care and Use Committee of the University of Florida and follow all applicable NIH guidelines.

2.2 Fear conditioning

Fear conditioning was performed two weeks before fMRI studies began. The fear conditioning system and methods used were previously described (Febo et al., 2024). The fear conditioning cages were housed in sound attenuation chambers. The chambers had computer-controlled lighting, white noise generator, a fan, and control units. These included audio speaker controls for tone generation, shock controllers for the internal cage floors, and infrared and white lighting controllers. The internal operant cage was made of translucent Plexiglas with a steel frame and steel shock grid floor connected to a computer controlled current stimulator (Med-Associates, Inc. St. Albans, VT). Activity within the fear conditioning cages was captured by a monochrome video camera. All cage accessories were controlled by PC running Video Freeze Software™. Camera lens brightness, gain, and shutter settings were verified and adjusted before collecting data and were kept constant across all mice. For each session, the detected motion-sensitive signals were

calibrated with the mouse inside the cage and NIR lights on. The estimated motion index was set to the same threshold level (10 a.u.) across all mice prior to data exporting or analyses. Videos were acquired at 30 frames per second (fps) with a minimum freeze duration of 30 frames. For training, on the first day a 180 second baseline was followed by four presentations of a 20 second tone (90 dB, 5kHz, 50ms risetime) with the presentation of moderate level current to the entire grid floor for 1 second (0.9mA) (inescapable shock) on the final second before the tone ended. Each of the four tone-shock presentations were separated by 190 seconds and the entire session lasted 17 minutes. On days 2 and 3 (recall tests at 24 and 48 h of training day 1, respectively), the same protocol was carried out in the absence of the electric shock. On day 3 (modified context test), the cage environment was modified by placing a plastic smooth white floor and diagonal walls, which covered the grid floor, light, and speaker. For each of the time epochs corresponding to the 4 tone-shock pairings, a component comprising a 20 second pre-shock tone interval and a 40 second post-shock interval were used to quantify percent component freezing (per day there were four 60 second components summed to provide total percent freezing per day). Motion-index was used as a measure of locomotor activity.

2.3 Magnetic resonance imaging instrumentation

Images were collected on a magnetic resonance spectrometer tuned to 470.7 MHz proton resonant frequency (Magnex Scientific 11.1 Tesla/40 cm horizontal magnet). The MR system was equipped with Resonance Research Inc. spatial encoding gradients (RRI BFG-240/120-S6, maximum gradient strength of 1000 mT/m at 325 Amps and a 200 µs risetime) and controlled by a Bruker AV3 HD console running Paravision 6.0.1 (Billerica, MA). An in house built 2 cm x 2.5 cm quadrature transceive surface radiofrequency (RF) was used for B1 signal generation and detection (RF engineering lab, Advanced Magnetic Resonance Imaging and Spectroscopy Facility, Gainesville, FL).

2.4 Mouse imaging setup

Mice were scanned sedated under a continuous paranasal flow of 0.25 % isoflurane gas (delivered at 0.04L/min mixed with medical grade air containing 70% nitrogen and 30% oxygen, Airgas, Inc.) and a continuous subcutaneous infusion of dexmedetomidine. Prior to setup, mice were anesthetized under 2% isoflurane and administered an intraperitoneal (i.p.) injection of 0.1mg/kg dexmedetomidine (at a 1ml/kg volume). Isoflurane was reduced to 0.25% throughout

the remaining imaging session. An infusion line was setup for subcutaneous delivery of dexmedetomidine over the course of scanning (0.1mg/kg/ml at an infusion rate of 25 µl/h using a PHD-Ultra microinfusion pump, Harvard Apparatus, Holliston, MA). Functional MRI scans were collected at least 50 minutes after the i.p. injection. Respiratory rates were monitored continuously, and body temperature was maintained at 36-37°C using a warm water recirculation system (SA Instruments, Inc., New York).

2.5 Functional MRI acquisition protocol

We acquired one T2 weighted anatomical and an fMRI scan per mouse. The T2-weighted Rapid Acquisition with Relaxation Enhancement (RARE) sequence was acquired with the following parameters: effective echo time = 41.4 ms, repetition time (TR) = 4 seconds, RARE factor = 16, number of averages = 12, field of view (FOV) of 15 mm x 15 mm and 0.8 mm thick slice, and a data matrix of 256 x 256 (0.06 μm^2 in plane) and 12 interleaved ascending coronal (axial) slices covering the entire brain from the rostral-most extent of the anterior prefrontal cortical surface, caudally towards the upper brainstem and cerebellum (acquisition time 9 minutes 36 seconds). Functional images were collected using a single-shot spin echo planar imaging sequence with the following parameters: TE = 16 ms, TR = 1.5 seconds, 600 repetitions, FOV = 15 x 15 mm and 0.9 mm thick slice, and a data matrix of 64 x 48 (0.23 x 0.31 µm in plane) with 14 interleaved ascending coronal slices in the same position as the anatomical scan. Ten dummy EPI scans were run prior to acquiring data under steady state conditions. Respiratory rates, isoflurane and dexmedetomidine delivery, body temperature, lighting, and room conditions were kept constant across subjects.

2.6 Image pre-processing

The image processing workflow followed previously published research (Colon-Perez et al., 2019; Febo et al., 2024; Kotlarz et al., 2022; Sadaka et al., 2023; Sakthivel et al., 2023). Resting state processing was carried out using Analysis of Functional NeuroImages (AFNI) (Cox, 1996), FMRIB Software Library (FSL) (Jenkinson et al., 2002), and Advanced Normalization Tools (ANTs) (Klein et al., 2009). Binary masks for anatomical and functional scans were created using ITKSNAP (Yushkevich et al., 2006). The brain binary masks were used for brain extraction prior to registration steps. Times series spikes were removed (3dDespike, AFNI), image repetition frames aligned to the first time series volume (3dvolreg, AFNI), and detrended (high pass filter

<0.009 Hz using AFNI 3dTproject). Independent component analysis (ICA) using Multivariate Exploratory Optimized Decomposition into Independent Components (FSL MELODIC version 3.0) was used to assess structured 'noise' or artefact components in each subject scan, in their native space. Most, if not all ICA components in this first stage contained artefact signal voxels along brain edges, in ventricles, and large vessel regions. These components were suppressed using a soft ('non-aggressive') regression approach, as implemented in FMRIB Software Library (FSL 6.0.5) using fsl_regfilt (Jenkinson et al., 2002). A low-pass filter (>0.12Hz) and spatial smoothing (0.4mm FWHM) was next applied to the fMRI scans prior to registration steps. Post-regression ICA was carried out to verify removal of artefact components and preliminary assessment of putative ICA networks in individual scans.

2.7 Atlas registration and resting state signal extraction

Anatomical scans were cropped and bias field corrected (N4BiasFieldCorrection, ANTs). Functional scans were cropped, and a temporal mean image was registered to the anatomical. Preprocessed anatomical and fMRI scans were aligned to a parcellated mouse common coordinate framework (version 3, or CCFv3) template (Wang et al., 2020). Bilateral region of interest (ROI)-based nodes (148 total) were created with the guidance of the annotated CCFv3 parcellation and using tools in ITKSNAP and FSL, similar to our previous work in rats (Pompilus et al., 2020; Yang et al., 2021). Large brain regions, such as hippocampus, motor, somatosensory, and visual cortices, were assigned multiple nodal masks. Thus, these are distinguished based on atlas coordinates and a numerical identifier at the end of the regional code (e.g., hippocampus contains nodes HPC1-HPC5). Anatomical images were linearly registered to the mouse template using FSL linear registration tool (FLIRT), using a correlation ratio search cost, full 180-degree search terms, 12 degrees of freedom and trilinear interpolation. The linear registration output was then nonlinearly warped to template space using ANTs (antsIntroduction.sh script). Anatomical-to-atlas linear and nonlinear transformation matrices were applied to fMRI scans at a later stage. Spontaneous signals, each with 600 data points, were extracted from 148 ROIs and used in cross-correlations and in calculations of Pearson r coefficients for every pairwise combinations of ROIs (using *corrcoef* function in MATLAB). The resulting number of pairwise correlations was 10,730 per subject (after removing 148 self-correlations). Correlation coefficients were Fisher's transform to ensure normality prior to statistical analyses. The center voxel coordinates for the ICA-based nodes normalized to the CCFv3 were used in 3D network visualizations using BrainNet viewer (Xia et al., 2013).

2.8 Network analysis

Weighted undirected matrices were analyzed using Brain Connectivity Toolbox (Rubinov and Sporns, 2010) in MATLAB (Mathworks, Natick, MA). Global graph metrics were calculated for edge density thresholds ranging from 2-40%. Global network measures for this density range were converted to area under the curve (AUC) values prior to statistical assessments. Node-specific network measures were converted to AUC values per node. We assessed several graph measures of network integration and communication efficiency in APP-PS1 and control mice. This included node strength (sum of edge weights/node) and degree (sum of edges/node) and global measures, such as transitivity (related to CC; number of triad groups normalized by all possible triad nodes in a network), and characteristic path length (CPL; the average edges or edge weights between node pairs). For local node efficiency, a length matrix was used to calculate inverse values in vicinity of a node, with added weights used to emphasize the highest efficiency node paths (Rubinov and Sporns, 2010; Wang et al., 2017). To corroborate results relative to random networks, all network measures were calculated on original and randomized versions of the functional connectivity matrices. Positive and negative edges were randomized by ~5 binary swaps with edge weights re-sorted at each step. A probabilistic approach for community detection was used to calculate a modularity statistic (Q), which indexes the rate of intra-group connections versus connections due to chance (Blondel et al., 2008). The procedure starts with a random grouping of nodes and iteratively moving nodes into groups which maximize the value of Q. The final number of modules and node assignments to each group (e.g., community affiliation assignments) was taken as the median of 100 iterations of the modularity maximization procedure (Pompilus et al., 2020). We analyzed the tendency of assortative vs dissortative mixing of nodes (Newman, 2002). The assortativity index is a correlation coefficient comparing node strength values between pairs of edge-connected nodes. Positive r values indicate connectivity between pairs of nodes with similar strengths (e.g., high strength nodes pairs with high and low with low), while negative r values indicate cross-pairings between low and high strength nodes. Functional connectivity networks were visualized in BrainNet viewer (Xia et al., 2013).

2.9 Immunohistochemical labeling of amyloid plaques and microglial cells

Mouse brains were harvested and processed for immunohistochemistry. Formalin fixed brain hemisections were paraffin embedded and sectioned sagittally using microtome at the following

Bregma locations: lateral 0.12mm, 1.56mm, and 3.25mm. Consecutive 4-µm were collected at each level for staining. The primary antibodies were Iba1 (1:1000, Wako Catalog # 019-19741) and 33.1.1 for staining Aβ plaques (1:13,000; provided by the Chakrabarty laboratory, Center for Translational Research on Neurodegenerative Diseases, University of Florida; kind gift of Todd E Golde, Emory University). Whole slides were scanned on a ScanScope XT Scanner (Leica Biosystems). Images were analyzed with tuned positivity algorithms for each respective stain using the Aperio ImageScope software.

2.10 Normalized gene counts and analysis of differentially expressed genes (DEGs)

BAM files were downloaded from Synapse.org as described (doi: https://doi.org/10.7303/syn2580853). Rsamtools and GenomicAlignments R packages (Lawrence et al., 2013; Morgan et al., 2023) were used to generate gene counts from the BAM files and were filtered for gene counts to remove genes with low counts (<10 genes). Subsequent analyses used normalized gene counts expressed as fragments per kilobase of transcript per million mapped reads (FPKM values). Analyses of DEGs was carried out using DESeq2 using default setting and a general linear model fit per gene (Love et al., 2014). Wald tests were used to compare TG vs NTG groups and multiple comparison adjustments of resulting p-values was done with the Benjamini-Hochberg false discovery rate (FDR) correction method. DEGs were defined as an absolute log2 fold change > 1 and an adjusted p value < 0.05 (visually evaluated as volcano plots). Gene annotation symbols were used to group genes according to their known expression in mouse brain cell types (Zhang et al., 2014). Within these cell type classifications, the geometric mean of the normalized gene counts for the genes comprising the cell types was calculated and analyzed between experimental groups. The cell type classifications included astrocytes, neurons, oligodendrocyte precursors, newly formed oligodendrocytes, myelinating oligodendrocytes, endothelial cells, and microglia/macrophage cells (Zhang et al., 2014).

2.11 Weighted Gene Co-Expression Network Analysis (WGCNA)

The WGCNA R package was used to construct gene correlation networks from the normalized expression data after filtering and removing genes with zero variance (Langfelder and Horvath, 2008, 2012). Plots of scale-free topology fitting and mean connectivity, both as a function of soft-threshold power values ranging from 1-20, were evaluated to select a gene network threshold using the “pickSoftThreshold” function. Networks were constructed all male and all female

samples separately. Adjacency matrices for a signed hybrid network were constructed using expression data and the chosen power threshold. The adjacency matrices were converted to topological overlap maps (TOMs) to be used for module network graphs. Hierarchical clustering was used to identify modules with the cutreeDynamic function. A deepSplit setting of two with a minimum module size of 30 was used for all analyses. Dendrograms were evaluated and compared by identifiable color-coded module statistics. Modules containing highly co-expressed genes were merged and co-expression similarity of entire modules were quantified by first calculating eigengenes and then clustering these based on their Pearson correlations. A cluster height cut was 0.25 (correlations of 0.75) was applied to merge similar modules. To quantify module-trait associations we recalculated module eigengene correlations and p values and displayed these as heat maps. Gene-trait and gene-module relationships were analyzed based on gene significance and module membership statistics. Module hub genes were determined with the 'chooseTopHubInEachModule' function.

For module preservation testing, female data were used as a reference and male data tested against the reference for low ($z < 2$), moderate ($z>2$, $z<10$), high module preservation ($z > 10$). We used sex as a comparison trait since preliminary assessments indicated sex differences in DEGs and cell type compositions. Statistics were run as multiExpr data for signed hybrid networks with 200 permutations and pariwise comparisons are made between common genes. Intramodule degree for eigengenes (kME) is used as a module membership statistic plotted against z score converted summary statistics determining significance. All statistical comparisons for preservation p values were Bonferroni corrected.

2.12 Statistical analysis

Statistical analyses and data visualization were carried out using tools in MATLAB, GraphPad Prism (version 10.2) or ggplot2 in the R statistics package. Unless otherwise stated, statistical analyses used either a two-way full factorial analysis of variance (ANOVA) (genotype x sex, critical $\alpha<0.05$) or Mann-Whitney tests. Post hoc tests used Tukey's honest significant difference (HSD) procedure. Where appropriate, FDR correction ($q \leq 0.05$) was used. Further analysis of fMRI scans was carried out using probabilistic ICA (Beckmann and Smith, 2004) as implemented in MELODIC Version 3.15, part of FSL (Beckmann and Smith, 2004; Hyvarinen, 1999) and as previously described for mouse fMRI scans (Febo et al., 2024). The resulting components were overlaid on the CCFv3 mouse atlas template and classified according to the peak z statistic anatomical location. A series of two-stage multiple linear regressions were used to back-project

group ICA components to subject-specific time courses (using spatial regressions) and spatial components (using temporal regressions). The subject-specific spatial component maps were then used in statistical comparisons for each component in the FSL randomise tool. The statistical design matrix was generated using the FSL Glm tool. We used a one-way ANOVA general linear model design. Randomization tests were carried out with 500 permutations (corrected p-level for significance is 0.05 and statistical thresholding of maps by threshold free cluster enhancement).

3. Results

3.1 Female APP-PS1 mice have a higher amount of amyloid plaques in basolateral amygdala and sensorimotor cortex than males

Histological analyses confirmed Aβ plaque presence across hippocampal, sensorimotor, prefrontal and basolateral amygdala regions in TG mice (Figure 1a and 1c). Additional analyses indicated that female TG mice had a greater amount of Aβ plaques in basolateral amygdala region (Mann-Whitney $p = 0.0087$)) and in neocortical areas corresponding to somatomotor cortex ($p = 0.035$) (Figure 1b). The hippocampus had a similar trend ($p =0.051$) and prefrontal cortex was not significantly different between male and females.

3.2 Amyloidosis increased functional connectivity within a posterior striatal/amygdala network

ICA identified 20 components that included previously reported networks (Bukhari et al., 2017; Febo et al., 2024; Jonckers et al., 2011; Sforazzini et al., 2014). These are summarized in Supplementary Figure 1. The components had peak z-statistic voxels in anterior and posterior cingulate, ventral and dorsal striatal, motor, somatosensory, visual cortices, thalamic, midbrain, and cerebellar regions. Statistical analysis using a two factor ANOVA (genotype x sex) indicated no significant main effects or interactions in established ICA networks. We analyzed an unclassified mixed network containing peak z score voxels in the left posterior striatum/basolateral amygdala (Figure 2a). This network included connectivity with cerebellar, prelimbic, motor, posterior cingulate, ventral hippocampus, entorhinal cortex regions. Two-way ANOVA revealed a main effect of amyloidosis, with TG mice having greater functional connectivity across these and other regions compared to NTG mice. No main effect of sex and sex x genotype interactions were observed for this mixed network (Figure 2b). Figure 2b summarizes the brain areas with greater functional connectivity in TG vs NTG mice. These included subregions of the motor cortex,

nucleus accumbens, insula, midbrain, piriform cortex, entorhinal cortex and reticular nuclei ($p < 0.05$, threshold free cluster enhanced corrected).

3.3 Amyloidosis is associated with higher eigenvector centrality scores in prefrontal and striatal subregions in female mice

Global network measures did not vary significantly between NTG and TG groups, regardless of sex (Supplementary Figure 2a). Figure 3a shows nodal eigenvector centrality scores calculated at 10% edge density. Eigenvector centrality scores at 10% edge density in several prefrontal and striatal nodes differed as a function of either sex or genotype (in the case of female mice) (Figure 3a). A similar difference was not observed in male mice, which had eigenvector centrality scores similar to TG female mice in these brain areas. TG females had higher eigenvector scores compared to NTG females in a single node in the left prelimbic cortex and two in the right prefrontal cortex, left lateral and ventral nodes in the orbital cortex, a node in the dorsomedial division of the left striatum (group[sex/genotype] x node interaction, $F_{441,3528}=1.2$, $p=0.005$; multiple between-group comparison t-tests per node with FDR adjusted p values at $q < 0.05$) (Figure 3a). NTG males had higher eigenvector scores compared to NTG females in the same nodes and also in left dorsal agranular insular cortex, right anterior cingulate cortex, right infralimbic cortex, right lateral orbital cortex, right secondary motor cortex, and right dorsomedial striatum (FDR adjusted $p < 0.05$ for comparisons across all nodes). When eigenvector scores were analyzed as AUC values per node, we also observed similar regions with lower eigenvector centrality scores in NTG compared to TG females and NTG females compared to NTG males (FDR adjusted $p < 0.05$ for comparison across all nodes). Node eigenvector centrality scores in prelimbic cortex, left lateral orbital cortex, left hippocampus, left dorsal agranular insula, left dorsolateral striatum were greater in TG compared to NTG female mice (Figure 3b). Eigenvector centrality in left and right prelimbic cortex, left hippocampus, right anterior cingulate cortex, and right orbital cortex were greater in NTG males than NTG female mice (Figure 3b). It should be noted that both left and right hemispheres of these brain regions had similar differences between male and female NTG and female NTG compared to female TG (with uncorrected p values < 0.05). However, only the mentioned brain regions were significant after FDR adjustment of p values. The summary 3D functional connectome maps in Figure 3c illustrate the average AUC eigenvector score brain distribution in each group.

3.4 Within-sex effects of amyloidosis on conditioned fear learning and recall

No between-group differences in fear learning were observed (Supplementary Figure 3). Both TG and NTG mice increased percent time freezing over the course of shock-tone exposure trials on the first day of testing (Supplementary Figure 3a). Comparison across days also failed to show any differences between NTG and TG mice on any days (Supplementary Figure 3b). No differences in motor activity were observed on any of the three test days (Supplementary Figure 3c). Within-subject analysis of day one of fear conditioning did reveal differences between groups, including sex differences. First, as expected, we observed an effect of trial on day 1 of testing (main effect of trial, $F_{3,72} = 8.8$, $p < 0.0001$). However, Tukey's multiple comparison test indicated that only male mice developed fear conditioning when comparing trials 3 and 4 to the first shock-cue pairing (NTG males: $p = 0.0047$ trial 1 vs. 3 and $p = 0.0017$ trial 1 vs. 4; TG males: $p = 0.03$ trial 1 vs. 3 and $p = 0.02$ trial 1 vs. 4). Percent time freezing in trials 3 and 4 compared to the first trial were not significant in NTG and TG female mice (Supplementary Figure 3a). Within-subject analyses also revealed significant differences in fear conditioning over the 3 test days (main effect of day, $F_{2,48} = 17.4$, $p < 0.0001$; Supplementary Figure 3b). Percent time freezing was maintained across days in NTG males. Male TG mice showed an increase in percent freezing time on days 2 and 3 relative to day 1 ($p = 0.0035$ and $p = 0.01$, respectively). Female NTG and TG mice both showed increases in percent time freezing on day 2 compared to day 1 (female NTG, $p = 0.0027$ for day 1 vs. 2; female TG, $p = 0.026$ for day 1 vs. 2). However, percent time freezing did not differ between day 3 (in a modified context) relative to day 1 in female NTG and TG mice. No differences in motor activity were observed within-group across days.

3.5 Unique neuronal and oligodendrocyte gene signatures associated with APP-PS1 familial AD mutations in female mice but not in males

Analysis of DEGs revealed a substantially elevated number of gene signatures in TG relative NTG female mice (Figure 4a). This included 216 upregulated and 24 downregulated genes (log2FC > 1.0, adjusted $p < 0.05$). DEGs in male mice included 54 upregulated and 5 downregulated genes (log2FC > 1.0, adjusted $p < 0.05$) (Figure 4b). We used two-way ANOVA to assess cell type composition for normalized gene counts, using geometric means as a composite measure for changes in cell type gene signatures (McFarland et al., 2021) (results for Tukey's post hoc tests are shown in Figure 4c). We observed significant differences in geometric means for microglial (genotype $F_{1,22} = 93.5$, $p <0.0001$), endothelial (sex $F_{1,22} = 12.78$, $p = 0.0017$) and vascular pericyte (sex $F_{1,22} = 5.8$, $p = 0.02$; genotype $F_{1,22} = 28.0$, $p < 0.0001$) genes in TG

vs NTG mice (Figure 4c, top row). Both male and female mice showed similar geometric means for these gene categories. Conversely, we observed reductions in geometric means for neuronal (genotype x sex $F_{1,22} = 8.25$, p= 0.0088) and myelinating oligodendrocyte (genotype x sex $F_{1,22} = 6.1$, p= 0.02; genotype $F_{1,22} = 8.9$, p= 0.0067) and newly formed oligodendrocyte (genotype x sex $F_{1,22} = 5.1$, p= 0.03; genotype $F_{1,22} = 13.1$, p= 0.0015) cell type categories in TG female mice relative to NTG females (Figure 4c, bottom row). A similar non-significant trend was observed for oligodendrocyte precursor category. This was not observed in male mice (Figure 4c, bottom row).

These results highlighted an interesting relationship between amyloid and neuronal and white matter related gene signatures, specific to female mice. WGCNA of RNAseq data revealed 10 modules with significant positively correlated genes and 7 modules with significant negatively correlated genes between TG vs NTG female mice (Figure 5a). Among the identified modules, we further analyzed gene signatures within the brown and lightblue4 modules (Figure 5b-c, respectively). The former is comprised of 669 positively correlated genes (r = 0.91, p = 1.87E-05), of which the top ten included genes related to immune activity (macrophage associated Cd68 was considered the 'hub' gene in this module). The latter module is comprised of 439 negatively correlated genes (r = -0.81, p = 6.8E-04), with the top10 most significant genes known for their roles in neuronal and behavioral functions (Gng7 was considered the 'hub' gene in this module). Statistical hierarchical cluster heatmaps in Figure 5d-e summarize comparisons within these two modules between TG and NTG female mice. This analysis illustrated a significant segregation of upregulated and downregulated gene clusters between NTG and TG female mice within each module.

Module preservation analysis indicated that the brown module containing positively correlated genes was highly preserved between male and female mice (Figure 6a-b). The lightblue4 module containing negatively correlated genes was moderately preserved in male relative to female mice (Figure 6a-b). Consistent with this result, analyses of normalized gene counts for the brown module showed significant increases for the first top 5 genes in both female and male mice (Figure 6c). These included Cd68 (genotype $F_{1,22} = 165$, $p < 0.0001$), Cd52 (sex x genotype $F_{1,22} = 6.6$, p = 0.02), Klhl6 (genotype $F_{1,22} = 126$, $p < 0.0001$), Irf8 (genotype $F_{1,22} = 93.6$, $p < 0.0001$), and Cd14(genotype $F_{1,22} = 27.5$, $p < 0.0001$). Analysis of normalized gene counts for the top ten gene signatures in the lightblue4 module indicated that these were significantly reduced only in APP-PS1 female mice relative to NTG female controls (Figure 6d). These included Gng7 (sex x genotype $F_{1,22} = 4.98$, p = 0.036), Syndig1l (sex x genotype $F_{1,22} = 8.7$, p = 0.0075), Pde1b (sex

x genotype $F_{1,22} = 8.5$, $p = 0.008$), Lrrc10b (sex x genotype $F_{1,22} = 7.8$, $p = 0.01$), Vps26b (genotype $F_{1,22} = 15.6$, $p = 0.0007$), and Ppp1r1b (sex x genotype $F_{1,22} = 9.9$, $p = 0.004$).

3.6 Amyloidosis is associated with similar microglia abundance in male and female mice

Our histopathological analysis also confirmed the presence of Iba1-labeled microglial cells, which appeared in greater abundance in TG compared to NTG mice (Supplementary Figure 4a). Iba1 labeling was greater in hippocampus ($p = 0.0004$), somatomotor ($p < 0.0001$) and prefrontal cortex ($p = 0.0008$) in male and female TG mice relative to their corresponding sex matched NTG controls (Supplementary Figure 4b).

4. Discussion

In this study we examined the effects of AD-amyloidosis on brain wide functional connectivity and gene expression in middle-aged mice. Our data reveal brain network and gene network correlates involved in the complex relationship between Aβ, functional connectivity, and cognitive/affective behavior in the APP-PS1 (line 85) mouse. These mice develop hippocampal Aβ deposits by 6 mo and abundant diffuse and dense core plaques throughout the cortex and hippocampus by 9 mo (Jankowsky et al., 2004). Based on substantial evidence of Aβ plaque induced changes in synaptic activity and plasticity in neocortical and hippocampal areas (Busche et al., 2019; Calvo-Flores Guzman et al., 2020; Dominguez-Alvaro et al., 2018; Kurucu et al., 2022; Lauterborn et al., 2021; Niraula et al., 2024; Petrache et al., 2019; Verret et al., 2012), we hypothesized functional connectivity differences as a result of amyloidosis in the APP-PS1 mouse. Surprisingly, functional connectivity in well-known mouse ICA networks (Bukhari et al., 2017; Grandjean et al., 2014a; Sforazzini et al., 2014; Shah et al., 2016), including somatosensory, motor, anterior and posterior cingulate cortices known to develop abundant extracellular plaques in this APP mouse strain (Whitesell et al., 2019), did not differ between TG and NTG mice. The lack of effects of amyloid on functional connectivity is likely due to the mechanism of Aβ aggregation in the APP-PS1 mouse. ΔE22Aβ mice with intracellular aggregation of Aβ and PSAPP mice with parenchymal plaque deposits showed either no differences in functional connectivity or exhibited mild differences compared to control mice (Grandjean et al., 2016). On the other hand, Arctic APP mice (ArcAβ) with vascular and intracellular Aβ aggregates had significantly reduced cortical functional connectivity in mice

(Grandjean et al., 2016). It will be important in future imaging studies to clarify how specific forms of Aβ aggregation affect neuronal circuit activity and large-scale functional connectivity networks.

Despite no observable effect of amyloid on established mouse ICA networks, we did observe differences in functional connectivity between NTG and TG mice within a mixed or unclassified striatal-amygdala network. Peak z-statistic values were observed in voxels located in posterior striatal-basolateral amygdala. The brain areas showing functional connectivity within this network included sensorimotor, cingulate, ventral hippocampal, midbrain and cerebellar regions. The diffuseness of the brain areas included in this ICA component somewhat parallel the similarly diffuse distribution of Aβ plaques in APP-PS1 mice. Within this ICA network, TG mice had higher functional connectivity than NTG mice in motor cortex, orbital cortex, insular cortex, temporal cortex, entorhinal cortex, dorsomedial striatum and midbrain. A shared feature of these brain areas is that they have either first or second order projections to or from the hippocampus, particularly ventral CA1 (Arszovszki et al., 2014; Ishikawa and Nakamura, 2006; Orsini et al., 2011; Swanson and Kohler, 1986; Thierry et al., 2000). A possible mechanism underlying the coactivation of structures in this ICA component, and the observed amyloid related differences in functional connectivity, is the compensatory plasticity of local circuits and projection neurons of ventral hippocampus that may occur in response to extracellular Aβ plaques (Bhembre et al., 2023). Such compensatory increases in functional connectivity are likely to fail at much later ages since prior evidence indicates that at 18 months of age interhemispheric fMRI connectivity is reduced in APP-PS1 male mice relative to C57BL6/J wildtype mice (Shah et al., 2013). We should note that hypersynchronous activity in parietal and temporal cortical areas were reported in 18-24 mo 3xTg-AD mice (Liu et al., 2018). This was correlated with tau but not Aβ burden (Liu et al., 2018). This result in 3xTg-AD mice differs from observations of Aβ associated hyperexcitability in fMRI connectivity in AD, which did not correlate with tau (Giorgio et al., 2024).

DEG analysis suggested that the observed differences in functional connectivity are linked to changes in neuroimmune activity, particularly microglia activation. Analyses of gene enrichment modules revealed gene clusters playing roles in the immune response, cell surface adhesion and receptor-mediated signaling, all elevated in conjunction with elevated human mutant APP in male and female mice. This was consistent with histological data showing similarly elevated microglial Iba1 immunostaining in cortical and hippocampal tissue in male and female TG mice. This is an expected result of amyloidosis, which has been reported in AD and across studies using APP mouse strains. It is also consistent with timelines of expression reported in *in vivo* PET studies of 12-13 mo APP-PS1 using radioligand with affinity for the translocator protein (TSPO) (Hu et al.,

2020). Interestingly, temporal cortical TSPO but not Iba1 follows a staged increase pattern similar to Aβ in immunolabeling studies of postmortem AD cases (Garland et al., 2023). Whether the elevated abundance in microglial cells contributes to the reorganization of functional connectivity is unclear. Microglial cells are known to play a phagocytic role in synaptic pruning (Giulian et al., 1995), particularly of unused or damaged dendritic spines (Wake et al., 2009), and this in turn may contribute to optimization of neural circuit processing (Giulian et al., 1995; Tremblay et al., 2010; Tremblay and Majewska, 2011; Zhan et al., 2014). Mice deficient of the Crx3cr1 chemokine receptor have reduced microglia and this is associated with reduced functional coherence between the prefrontal cortex and hippocampus and reduced functional connectivity (Zhan et al., 2014). Crx3cr1 knockout mice also exhibit reduced synapses in adult born dentate gyrus cells along with structural changes in neurons within this region (Bolos et al., 2018). Iba1 deficiency in the Allograph inflammatory factor1 (Aif1) knock mouse reduces hippocampal CA1 spines and pyramidal firing frequencies (Lituma et al., 2021). Conversely, lifelong depletion of microglia in mice with deletion of the fms-intron regulatory element (Csfr1$^{\Delta FIRE/\Delta FIRE}$ mice) showed no differences in the number of excitatory and inhibitory synapses nor spine density in the hippocampal CA1, although neurons within this region did show deficits in excitability and altered synaptic properties (Surala et al., 2024).

The observed Aβ related changes in functional connectivity and DEGs were not accompanied by differences in fear conditioning between TG and NTG mice, which was unexpected given previous behavioral characterization of the APP mouse (Janus et al., 2015; Kilgore et al., 2010; Lalonde et al., 2005). We did not observe differences between NTG and TG mice on any of the test days, although a trend towards lower freezing responses in male TG mice was observed on day 1. This finding suggests that the observed brain functional connectivity and gene expression changes might precede the effects of Aβ on cognitive and emotional behaviors. It is worth noting that changes in functional connectivity and AB plaque related PET signals have been reported in elderly individuals without cognitive deficits (Hedden et al., 2009; Lim et al., 2014). Although this seems plausible in the present mouse imaging study, there are alternative explanations for the lack of differences in fear conditioning that requires consideration. The combined classical-contextual fear conditioning assay (tone-context-shock pairing) and the moderate-to-high current level for shock delivery used in the present study could account for differences relative to previous work using a standard contextual fear conditioning assay (context-shock pairing) (Janus et al., 2015). As discussed in recent work by our group (Febo et al., 2024), age- and strain-related declines in sensorimotor function can impact performance on fear conditioning assays and the outcomes may reflect underlying mechanisms not directly related to impaired learning and

memory. The hybrid classical-contextual fear conditioning assay using auditory plus contextual cues, and a higher moderate current level, was used here to induce a robust learning and memory performance in APP-PS1 mice. However, this approach could have masked milder cognitive declines observed in previous work using contextual cues only (Janus et al., 2015).

Our results reveal significant sex dependent effects of amyloidosis on histopathological, gene expression, functional brain activation and fear conditioning measurements. We observed sex differences in eigenvector centrality, a measure of node 'hubness', which was differentially altered by amyloidosis in female compared to male mice. The brain regions with highest eigencentrality in both male and females included the anterior thalamus, dorsal striatum and areas of medial prefrontal cortex and orbital cortex (illustrated in Figure 5c). Functional connectome eigenvector centrality was lower in several prefrontal areas and striatum of NTG female mice relative to NTG males. Sex differences in centrality in functional connectivity networks have been reported in human cortex (Zuo et al., 2012) but in no other rodent fMRI studies to date. In humans, women reportedly have higher eigenvector centrality scores in hippocampus and posterior cingulate cortex than men (Zuo et al., 2012). We tested another centrality measure, betweenness centrality, which on average resulted in essentially identical distribution of node betweenness centrality rankings across male and female mice. This suggests that the observed sex differences in eigencentrality are not generalized to other network centrality measures. It is unclear if this topological organization has a neurophysiological underpinning relevant to cognitive or emotional states in humans and other species.

APP female mice had higher eigenvector centrality values in prefrontal cortical regions than controls. Indeed, eigenvector centrality in APP female mice were comparable to TG and NTG male mice. This may have significance to female-specific effects of amyloid in modulating the functional and behavioral roles of prefrontal brain regions. This is supported by research showing that PET-based amyloid positivity is related to increased eigenvector centrality in prefrontal cortex, even in the absence of declines in cognitive performance (Lorenzini et al., 2023). The link between amyloid positivity and eigenvector centrality in cognitively healthy controls appears to be relatively specific to the default mode network (Ingala et al., 2021; Lorenzini et al., 2023). The increased eigenvector centrality observed in posterior and mid-cingulate cortical regions correlates with elevated cerebral spinal fluid (CSF) markers of Aβ and phosphorylated tau (p-tau) (Skouras et al., 2019) and this in turn relates to cognitive impairment (Skouras et al., 2019). Others have reported differences in eigenvector centrality linked to stable versus progressive mild cognitive impairment (Qiu et al., 2016). Eigenvector centrality in the lateral superior temporal

gyrus changes with age and may inform on cognitive decline in MCI (Zhang et al., 2024). Overall, there is evidence from human neuroimaging studies supporting the observed sex differences in eigenvector centrality and a potentially important link between this network measure and amyloidosis.

In support of the observed effects of amyloidosis on eigenvector centrality in female mice, we found that amyloidosis decreased a cluster of genes specifically in female mice. While the amyloid and immune related genes were highly preserved in modular analyses, the gene clusters reduced in APP-PS1 females was moderately preserved when comparing to male mice. This female specific pattern of gene expression changes included Gng7, Syndig1l, Pde1b, Lrrc10b, Vps26b as the top 5 downregulated genes in APP females, and Gad1 (glutamic acid decarboxylase 1 gene encoding the main enzyme involved in producing GABA in neurons) within the top 10 downregulated genes. *Gad1* is also known as Gad67 and is found widely distributed in inhibitory interneuron cell soma (Stone et al., 1999). AD associated alterations in GABAergic neuron function and structure in hippocampal, temporal and parietal regions are well published (Fuhrer et al., 2017; Kurucu et al., 2022). Aβ is linked to hypersynchronous field potential activity in mice via a voltage gated sodium channel – Nav1.1, mechanism in Gad67-expressing parvalbumin interneurons in parietal cortex of mice (Verret et al., 2012). An intriguing notion is that lightblue4 module genes are linked to functional dysregulation or loss of GABAergic neurons in response to Aβ, specifically in female mice. *Gng7* reportedly harbors differentially methylated positions associated with Braak stage pathology (Li et al., 2020) and in mice has been causally linked to ischemic stroke induced motor dysfunction and stressor-induced anxiety (Halder et al., 2020) and striatal adenosine-A_{2A} receptor-containing medium spiny neurons' (MSNs) control over locomotor responses to psychostimulants (Brunori et al., 2021). Interestingly, *Gng7* is one of the target genes of microRNAs, miR-881-3p and miR-504, that are downregulated by alcohol treatment in female but not male rats (Choi et al., 2020). *Syndig1l* harbors epigenetic CpG-related single nucleotide polymorphisms associated with AD in Hispanic populations (Ma et al., 2024). *Pde1b*, encoding a phosphodiesterase 1, has been linked to motor activity and spatial learning (Reed et al., 2002), identified in motor control in striatum of transgenic mice of Huntington's (Hebb et al., 2004) and involved in depression-like behaviors in response to stress in mice (Hufgard et al., 2017). Overexpression of *Pde1b* in dopamine D1 receptor-containing striatal MSNs attenuated the locomotor response to cocaine in female mice but not males (Teague et al., 2024). *Ppp1r1c* also known as Darpp32, is found in dopamine receptor D1 expressing striatal medium spiny neurons (Ouimet and Greengard, 1990). Darpp32 follows a sex-dependent pattern of expression (Weiner et al., 2009; Zhou et al., 2009) and its expression has been shown to be altered by

estradiol (Stroppolo et al., 2004). These new data offer useful insight into potential avenues to investigate sex-specific and hormonally regulated mechanisms of amyloid aggregation that may differentially impact female brains compared to males.

Finally, we observed a higher number of extracellular plaques in female versus male mice. This was observed in somatomotor cortex and basolateral amygdala. These findings are consistent with previous research using the APP-PS1 mouse (Wang et al., 2003; Wu et al., 2016), the Tg2576 (Lee et al., 2002) and the triple transgenic AD mouse (3xTg-AD) (Hirata-Fukae et al., 2008). The hippocampal concentrations of Aβ40 and Aβ42 and number of plaques at 12 and 17 mo is more than twice the amount in females compared to male APP-PS1 (Wang et al., 2003). The mechanism leading to higher plaque numbers in female versus male mice may involve effects of estrogen loss on Aβ overproduction. Ovariectomy increases Aβ levels in female Tg2576 mice (measured in whole brain homogenates by mass spectrometry), and estrogen replacement reduces Aβ to sham Tg2576 control levels (Zheng et al., 2002). In that study, estrogen did not appear to alter full length human APP, secreted APP nor the PS1 C-terminal fragment (Zheng et al., 2002). A similar increase in Aβ load following OVX, and a reduction with estrogen treatment, is observed in CA1, subiculum and frontal cortex of 3xTg-AD mice (Carroll et al., 2007). Estrogen appears to repress BACE1 gene expression, and its activity, via estrogen receptor alpha (Cui et al., 2022), a mechanism that may underlie the higher number of Aβ plaques in APP female versus male mice (Zheng et al., 2002). Results for gene enrichment analysis further substantiated the observed sex differences in amyloid expression, unexpectedly revealing a diametrically opposed App gene levels compared to the histological data. App gene counts were higher in males compared to female mice, whereas the opposite was found with Aβ plaque immunolabeling. This is consistent with a reduction App gene expression in TG females as a result of putative estrogenic repression of BACE1 (Cui et al., 2022).

5. Conclusions

To conclude, the present study adds to the literature on the functional network changes in response to increased presence of extracellular plaques. Reducing extracellular plaque pathology could be one way in which neuronal communication might be safeguarded in individuals at risk of cognitive decline and Alzheimer disease. Moreover, the identified functional connectome marker, specific to APP-PS1 females and consistent with the human literature, will be interesting to further investigate in other APP strains. As indicated above, nuanced mechanisms of Aβ aggregation may be important to understand in terms of how this impacts broader network activity.

Figures and legends

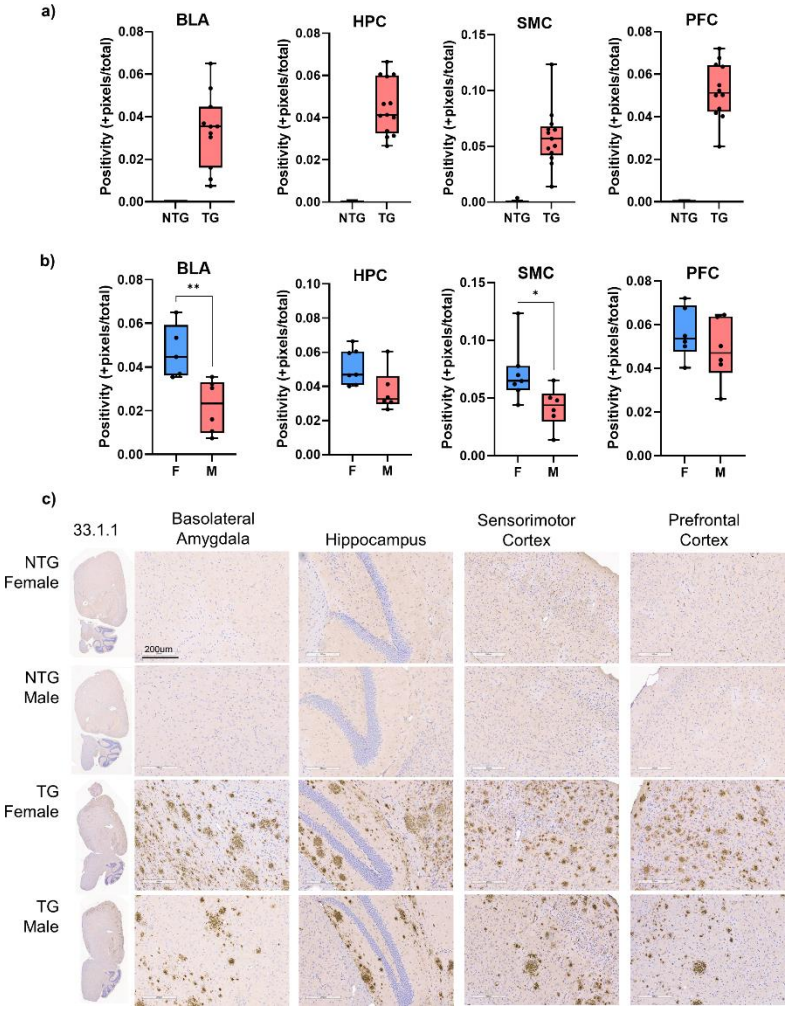

Figure 1. Female APP-PS1 mice have a greater number of amyloid plaques in basolateral amygdala and somatomotor neocortical areas compared to male APP-PS1 mice. a) Confirmation of amyloid plaque presence in TG mice using antibody 33.1.1. b) Comparison of amyloid plaque burden between male (M) and female (F) TG mice. c) Representative histological sections from female and male NTG and TG mouse basolateral amygdala (BLA), prefrontal cortex (PFC), somatomotor cortex (SMC), and hippocampus (HPC). Data in a-b are box-whisker showing median, minimum-maximum values and individual data points. Asterisks are *$p < 0.05$, **$p < 0.01$.

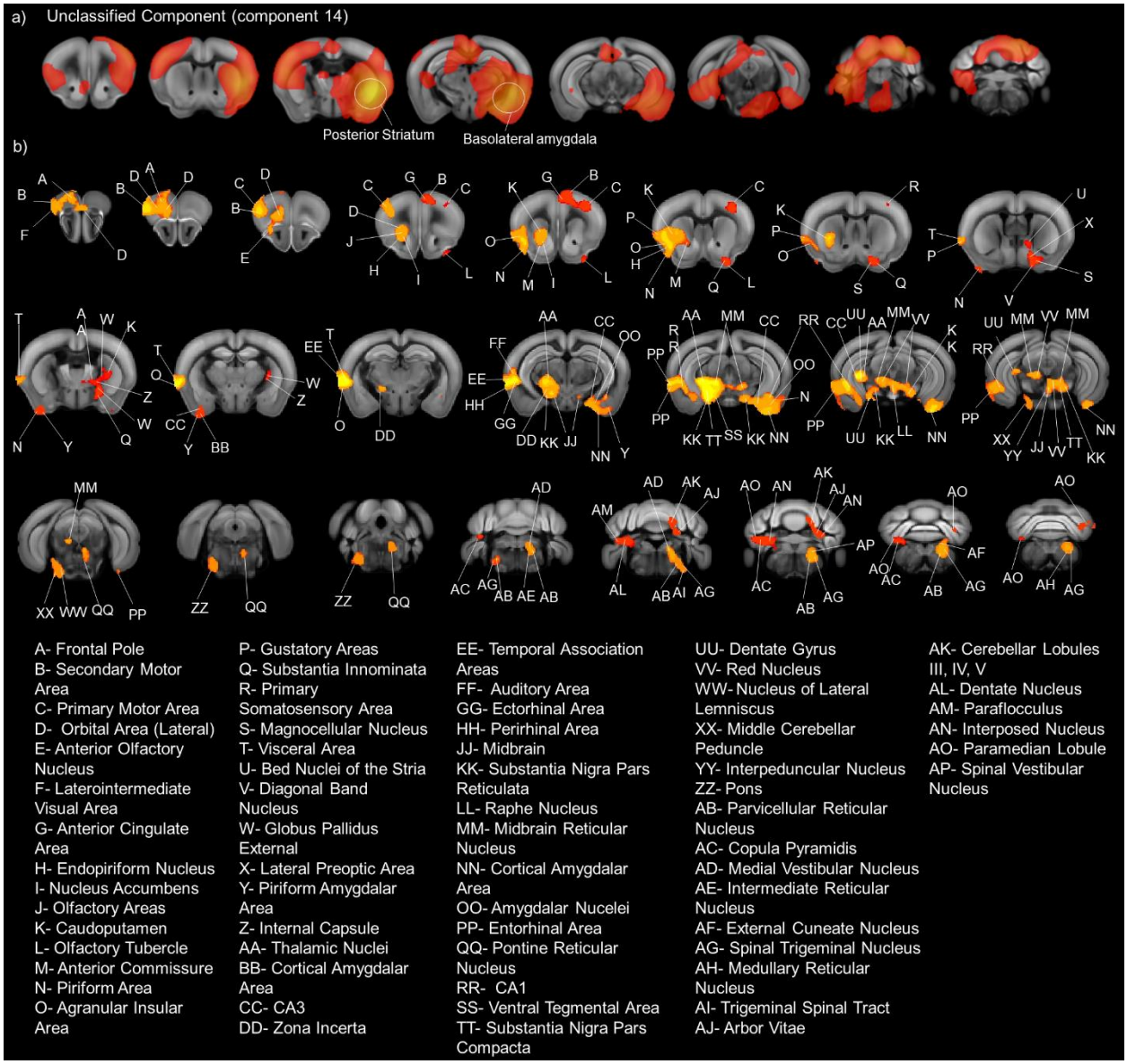

Figure 2. Amyloidosis increased functional connectivity within an unclassified component that included nodes in posterior dorsal striatum and basolateral amygdala in both male and female mice. a) Undistinct component measured in a cohort of 28 NTG and TG fMRI scans. Higher intensity/higher functional connectivity voxels in yellow are encircled and indicated by the corresponding brain region. b) Statistical results of full factorial ANOVA assessing genotype x sex interactions and main effects ($p < 0.05$, corrected). Letter codes indicate the brain area according to the Allen Mouse Brain Common Coordinate Reference atlas (CCFv3). Brain area names are matched to letter codes at the bottom of the figure. Significant voxels (main effect genotype) are highlighted in yellow-orange hue indicating TG > NTG.

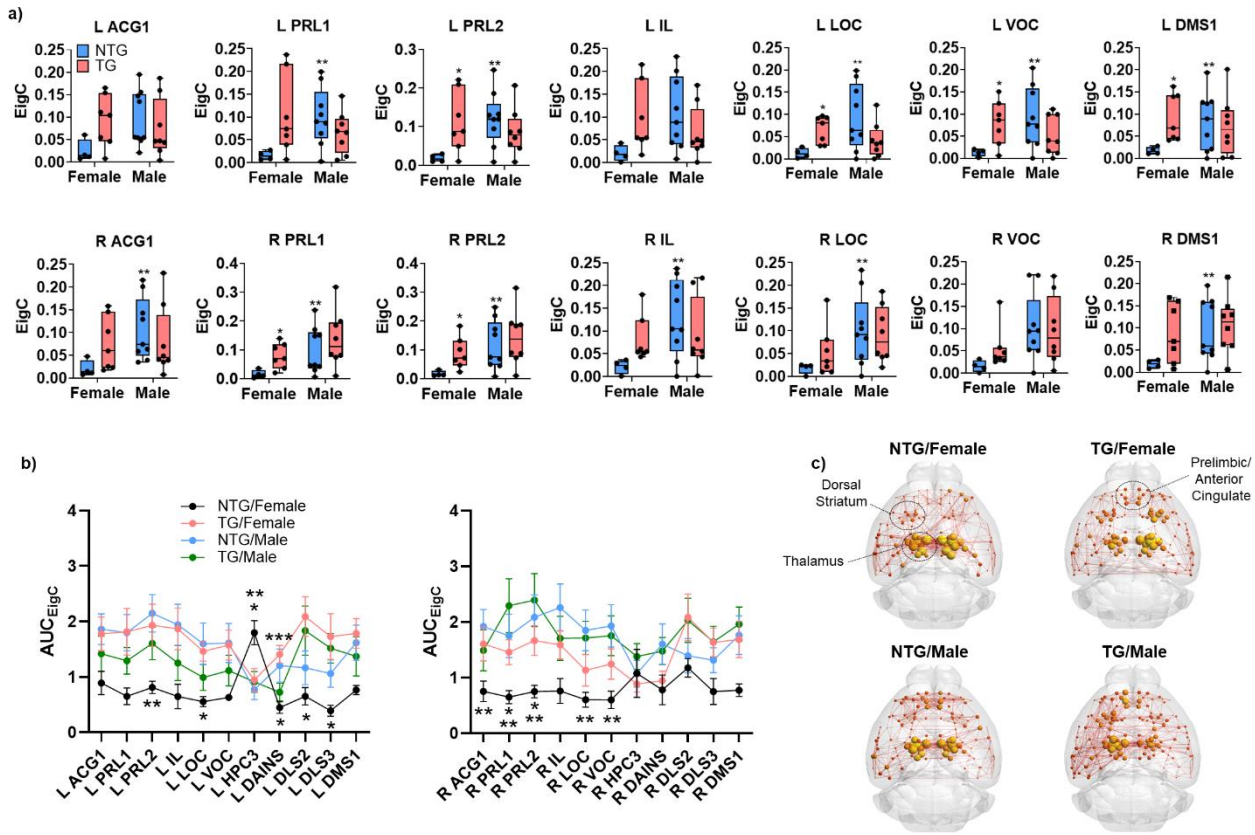

Figure 3. Sex specific effects of amyloid on functional network 'hub' topology. a) Eigenvector centrality scores for several prefrontal cortical and striatal nodes calculated for a 10% network density. Data in box-whisker plot are median with minimum and maximum values and show individual data points. Top row plots show ROI data for left (L) hemisphere and bottom row plot the right (R) hemisphere. b) Area under the curve (AUC) values calculated for eigenvector centrality across multiple edge densities (2-40%) per ROI. Data in plot is presented as mean standard ± error. Left plot shows ROI data for left (L) hemisphere and right plot the right (R) hemisphere. c) Connectome maps represent mean AUC values for eigenvector centrality per node and edge strength (Pearson correlations) as spherical nodes and lines connecting nodes. Node eigenvector centrality is reflected in sphere size and color intensity. Edges are thresholded at 6% density for visual purposes. Asterisks indicate significantly difference between NTG vs TG females* and NTG females vs males**. Abbreviations: ACG1, anterior cingulate gyrus; PRL, prelimbic cortex; IL, infralimbic cortex; LOC, lateral orbital cortex; VOC, ventral orbital cortex; DMS, dorsomedial striatum.

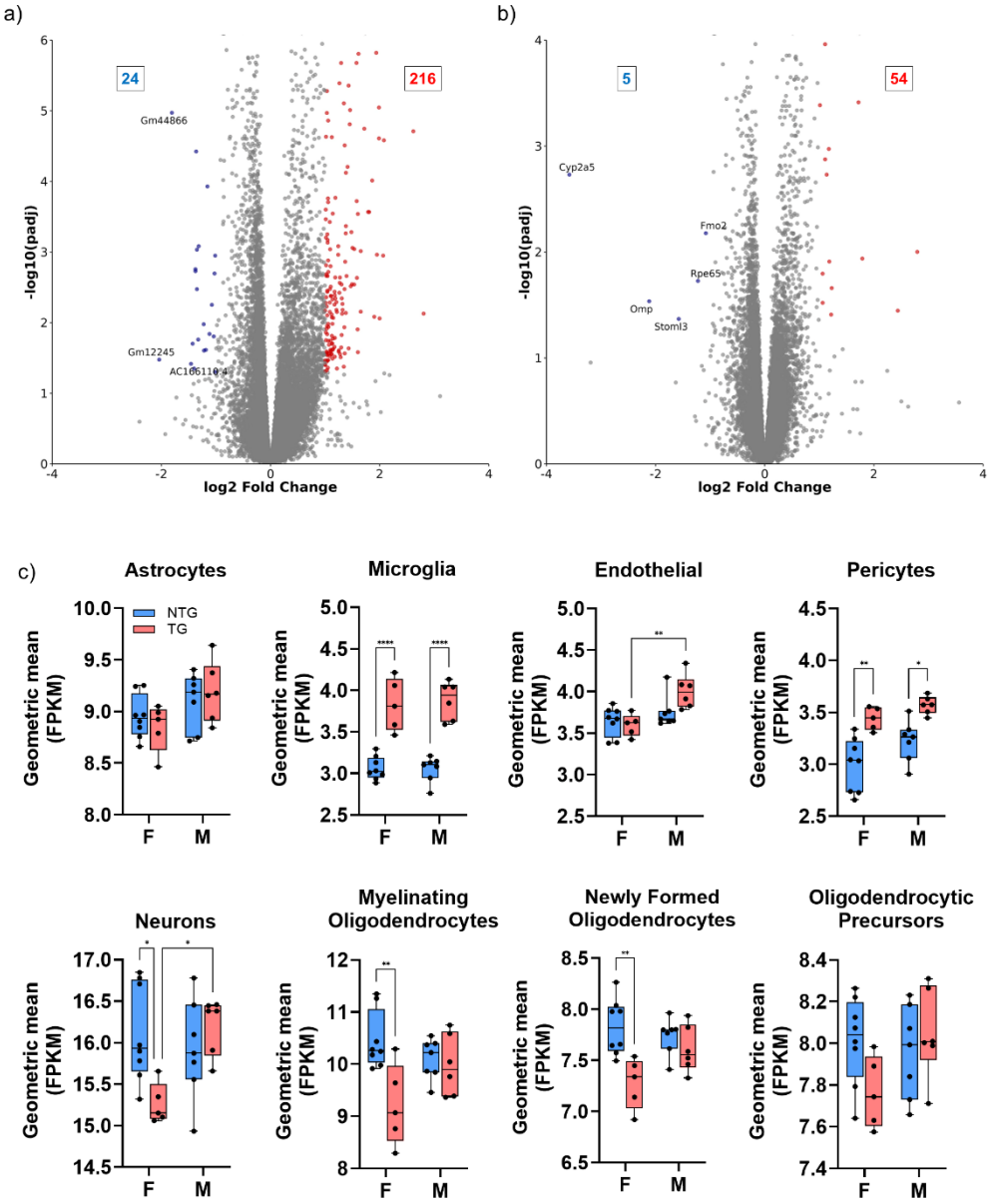

Figure 4. Diverging patterns in differentially expressed genes (DEGs) in female and male APP-PS1 mice. a) Volcano plot showing significant downregulated (blue numbers) and upregulated (red numbers) DEGs as a function of APP-PS1 genotype in female mice. b) Volcano plot of DEGs in male mice. c) Comparison of gene expression signatures for cell type composition groupings between NTG and TG female (F) and male (M) mice. Data are shown as box-whisker with median, minimum-maximum values and individual data points. Asterisks are *p < 0.05, **p < 0.01, *** p < 0.001.

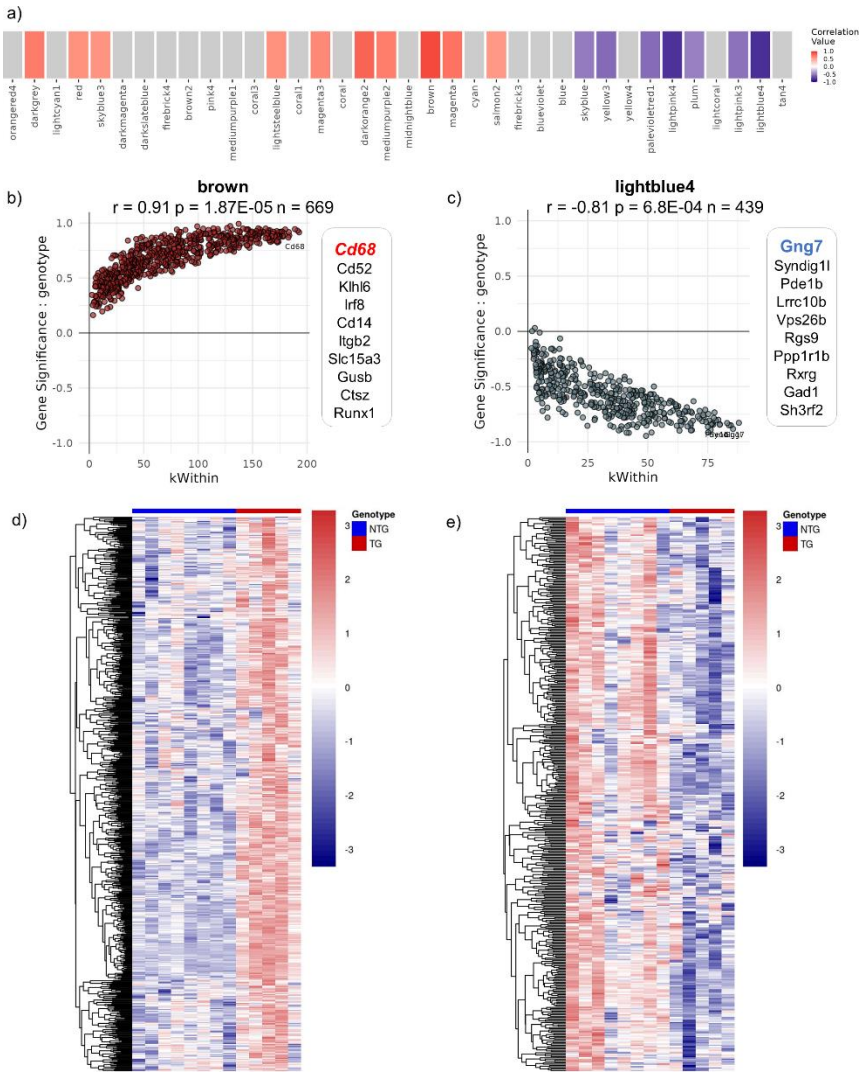

Figure 5. Weighted gene correlation network analysis identified two distinct modules in female APP-PS1 brain with significant positively and negatively correlated groups of immune and neuronal genes. a) Heatmap showing modules with gene networks that are positively (red) and negatively (blue) correlated with genotype (modules with p-value less than 0.1 are indicated by color). Modules with nonsignificant correlations are in grey. b) Gene significance by within module degree (kWithin) for the brown module (evaluated for genotype). Listed are the top 10 most significant genes with hub gene colored red. c) Gene significance by within module degree (kWithin) for the lightblue4 module (evaluated for genotype). Listed are the top 10 most significant genes with hub gene colored blue. d) Hierarchical clustering of gene expression in brown module. e) Hierarchical clustering of gene expression in lightblue4 module.

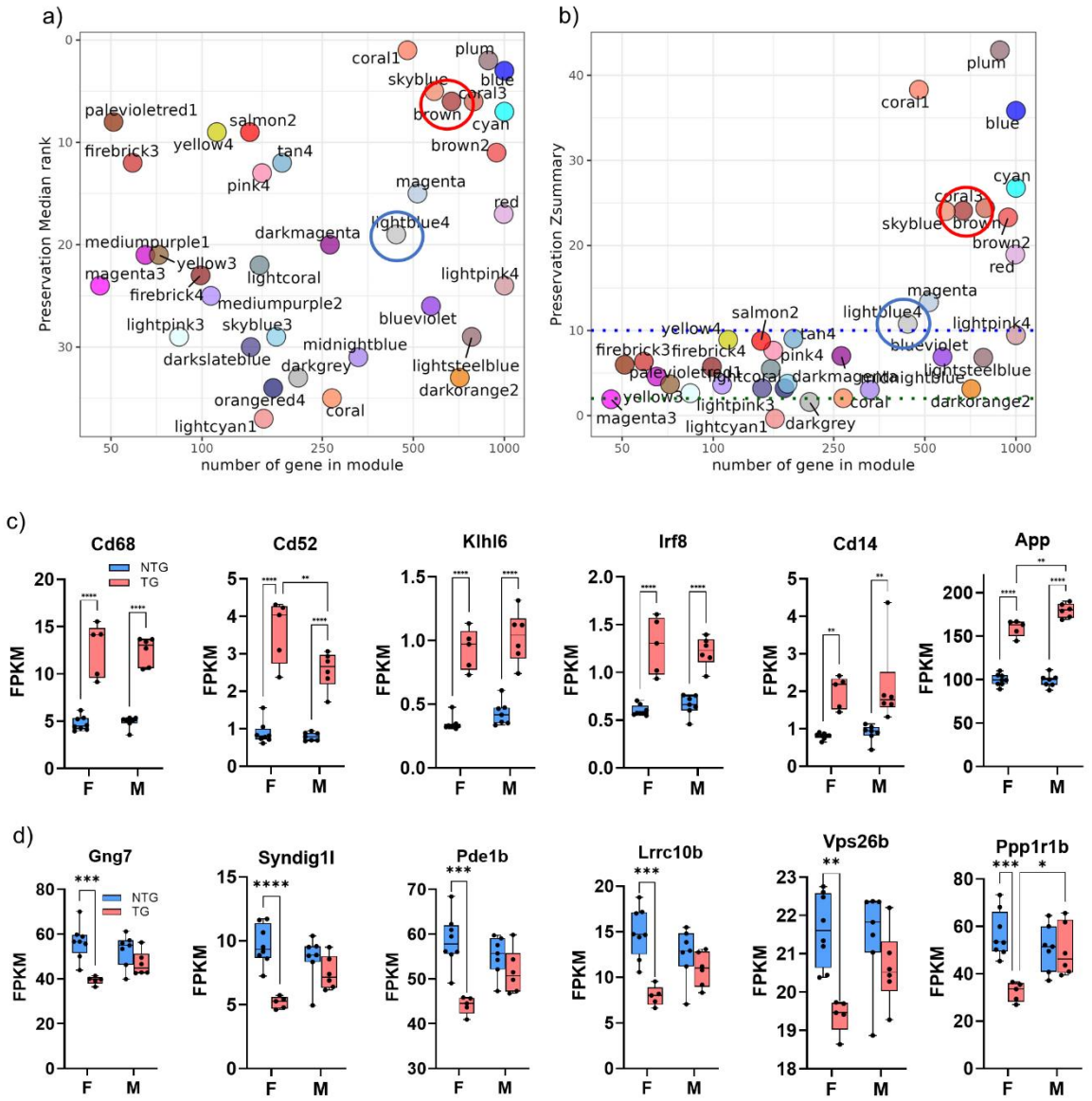

Figure 6. High module preservation of DEGs involved in immune responses (brown module) and moderate preservation of DEGs involved in neuronal function and structure (lightblue4 module). Female module DEGs used as reference to test male DEGs. A) Module rank. Modules close to 0 are highly preserved. B) Zsummary plot. Moderate preservation Z = 2-10 and high preservation Z > 10. d) Comparison of normalized gene expressions for the top 5 most significant genes in the brown module. App gene included as a comparison. e) Comparison of normalized gene expressions for the top 5 most significant genes in the brown module. Ddx3x gene with sex dependent expression levels is included as a comparison. Data are shown as box-whisker with median, minimum-maximum values and individual data points. Asterisks are *p < 0.05, **p < 0.01, *** p < 0.001, ****p < 0.0001.

Acknowledgements

The authors would like to thank Marjory Pompilus for her help with portions of the work. Marcelo Febo thanks for the support provided by the McKnight Brain Institute of the University of Florida. Zachary Simon received support from the McKnight Brain Institute of the University of Florida to present a preliminary version of this work at the Annual Meeting of the Society for Neuroscience. The TAUAPPms RNAseq datasets used in this manuscript has been previously deposited in AD Knowledge Portal (https://adknowledgeportal.org) with the support of NIH/NIA (U01 AG046139 to T.E. Golde, N.D. Price, and N. Ertekin-Taner). The data can be accessed at https://www.synapse.org/ (Synapse ID:syn2580853). The AD Knowledge Portal is a platform for accessing data, analyses, and tools generated by the Accelerating Medicines Partnership (AMP-AD) Target Discovery Program and other National Institute on Aging (NIA)-supported programs to enable open-science practices and accelerate translational learning.

Funding

This work was funded by NIA R21AG065819 with additional support provided by the McKnight Brain Institute of the University of Florida. The neuroimaging components of this work were performed in the National High Magnetic Field Laboratory's AMRIS Facility, which is funded by National Science Foundation Cooperative Agreement No. DMR-1644779 and the State of Florida. The original funding for the mouse brain RNA sequencing studies downloaded from AD Knowledge Portal was provided by the NIH U01 AG046139 to Drs. Todd E Golde, Nilufer Taner and Nathan Price.

References

Adriaanse, S.M., Binnewijzend, M.A., Ossenkoppele, R., Tijms, B.M., van der Flier, W.M., Koene, T., Smits, L.L., Wink, A.M., Scheltens, P., van Berckel, B.N., Barkhof, F., 2014. Widespread disruption of functional brain organization in early-onset Alzheimer's disease. PLoS One 9(7), e102995.

Alzheimer's Association, 2022. 2022 Alzheimer's disease facts and figures. Alzheimers Dement 18(4), 700-789.

Arszovszki, A., Borhegyi, Z., Klausberger, T., 2014. Three axonal projection routes of individual pyramidal cells in the ventral CA1 hippocampus. Front Neuroanat 8, 53.

Beckmann, C.F., Smith, S.M., 2004. Probabilistic independent component analysis for functional magnetic resonance imaging. IEEE Trans Med Imaging 23(2), 137-152.

Bhembre, N., Bonthron, C., Opazo, P., 2023. Synaptic Compensatory Plasticity in Alzheimer's Disease. J Neurosci 43(41), 6833-6840.

Blondel, V.D., Guillaume, J.-P., Lambiotte, R., Lefebvre, E., 2008. Fast unfolding of communities in large networks. Journal of Statistical Mechanics: Theory and Experiment 2008, 2-12.

Bolos, M., Perea, J.R., Terreros-Roncal, J., Pallas-Bazarra, N., Jurado-Arjona, J., Avila, J., Llorens-Martin, M., 2018. Absence of microglial CX3CR1 impairs the synaptic integration of adult-born hippocampal granule neurons. Brain Behav Immun 68, 76-89.

Brunori, G., Pelletier, O.B., Stauffer, A.M., Robishaw, J.D., 2021. Selective Manipulation of G-Protein gamma(7) Subunit in Mice Provides New Insights into Striatal Control of Motor Behavior. J Neurosci 41(44), 9065-9081.

Buckner, R.L., Sepulcre, J., Talukdar, T., Krienen, F.M., Liu, H., Hedden, T., Andrews-Hanna, J.R., Sperling, R.A., Johnson, K.A., 2009. Cortical hubs revealed by intrinsic functional connectivity: mapping, assessment of stability, and relation to Alzheimer's disease. J Neurosci 29(6), 1860-1873.

Bukhari, Q., Schroeter, A., Cole, D.M., Rudin, M., 2017. Resting State fMRI in Mice Reveals Anesthesia Specific Signatures of Brain Functional Networks and Their Interactions. Front Neural Circuits 11, 5.

Busche, M.A., Wegmann, S., Dujardin, S., Commins, C., Schiantarelli, J., Klickstein, N., Kamath, T.V., Carlson, G.A., Nelken, I., Hyman, B.T., 2019. Tau impairs neural circuits, dominating amyloid-beta effects, in Alzheimer models in vivo. Nat Neurosci 22(1), 57-64.

Cacace, R., Sleegers, K., Van Broeckhoven, C., 2016. Molecular genetics of early-onset Alzheimer's disease revisited. Alzheimers Dement 12(6), 733-748.

Calvo-Flores Guzman, B., Kim, S., Chawdhary, B., Peppercorn, K., Tate, W.P., Waldvogel, H.J., Faull, R.L., Montgomery, J., Kwakowsky, A., 2020. Amyloid-Beta(1-42) -Induced Increase in GABAergic Tonic Conductance in Mouse Hippocampal CA1 Pyramidal Cells. Molecules 25(3).

Canu, E., Agosta, F., Mandic-Stojmenovic, G., Stojkovic, T., Stefanova, E., Inuggi, A., Imperiale, F., Copetti, M., Kostic, V.S., Filippi, M., 2017. Multiparametric MRI to distinguish early onset Alzheimer's disease and behavioural variant of frontotemporal dementia. Neuroimage Clin 15, 428-438.

Carroll, J.C., Rosario, E.R., Chang, L., Stanczyk, F.Z., Oddo, S., LaFerla, F.M., Pike, C.J., 2007. Progesterone and estrogen regulate Alzheimer-like neuropathology in female 3xTg-AD mice. J Neurosci 27(48), 13357-13365.

Choi, M.R., Han, J.S., Jin, Y.B., Lee, S.R., Choi, I.Y., Lee, H., Cho, H., Kim, D.J., 2020. Differential expression of microRNAs in the hippocampi of male and female rodents after chronic alcohol administration. Biol Sex Differ 11(1), 65.

Cochran, J.N., McKinley, E.C., Cochran, M., Amaral, M.D., Moyers, B.A., Lasseigne, B.N., Gray, D.E., Lawlor, J.M.J., Prokop, J.W., Geier, E.G., Holt, J.M., Thompson, M.L., Newberry, J.S., Yokoyama, J.S., Worthey, E.A., Geldmacher, D.S., Love, M.N., Cooper, G.M., Myers, R.M., Roberson, E.D., 2019. Genome sequencing for early-onset or atypical dementia: high diagnostic yield and frequent observation of multiple contributory alleles. Cold Spring Harb Mol Case Stud 5(6).

Colon-Perez, L.M., Ibanez, K.R., Suarez, M., Torroella, K., Acuna, K., Ofori, E., Levites, Y., Vaillancourt, D.E., Golde, T.E., Chakrabarty, P., Febo, M., 2019. Neurite orientation dispersion and density imaging reveals white matter and hippocampal microstructure changes produced by Interleukin-6 in the TgCRND8 mouse model of amyloidosis. Neuroimage 202, 116138.

Cox, R.W., 1996. AFNI: software for analysis and visualization of functional magnetic resonance neuroimages. Comput Biomed Res 29(3), 162-173.

Cui, J., Ait-Ghezala, G., Sambamurti, K., Gao, F., Shen, Y., Li, R., 2022. Sex-Specific Regulation of beta-Secretase: A Novel Estrogen Response Element (ERE)-Dependent Mechanism in Alzheimer's Disease. J Neurosci 42(6), 1154-1165.

D'Argenio, V., Sarnataro, D., 2020. New Insights into the Molecular Bases of Familial Alzheimer's Disease. J Pers Med 10(2).

Dominguez-Alvaro, M., Montero-Crespo, M., Blazquez-Llorca, L., Insausti, R., DeFelipe, J., Alonso-Nanclares, L., 2018. Three-dimensional analysis of synapses in the transentorhinal cortex of Alzheimer's disease patients. Acta Neuropathol Commun 6(1), 20.

Eissman, J.M., Dumitrescu, L., Mahoney, E.R., Smith, A.N., Mukherjee, S., Lee, M.L., Scollard, P., Choi, S.E., Bush, W.S., Engelman, C.D., Lu, Q., Fardo, D.W., Trittschuh, E.H., Mez, J., Kaczorowski, C.C., Hernandez Saucedo, H., Widaman, K.F., Buckley, R.F., Properzi, M.J., Mormino, E.C., Yang, H.S., Harrison, T.M., Hedden, T., Nho, K., Andrews, S.J., Tommet, D., Hadad, N., Sanders, R.E., Ruderfer, D.M., Gifford, K.A., Zhong, X., Raghavan, N.S., Vardarajan, B.N., Alzheimer's Disease Neuroimaging, I., Alzheimer's Disease Genetics, C., Team, A.S., Pericak-Vance, M.A., Farrer, L.A., Wang, L.S., Cruchaga, C., Schellenberg, G.D., Cox, N.J., Haines, J.L., Keene, C.D., Saykin, A.J., Larson, E.B., Sperling, R.A., Mayeux, R., Cuccaro, M.L., Bennett, D.A., Schneider, J.A., Crane, P.K., Jefferson, A.L., Hohman, T.J., 2022. Sex differences in the genetic architecture of cognitive resilience to Alzheimer's disease. Brain 145(7), 2541-2554.

Febo, M., Mahar, R., Rodriguez, N.A., Buraima, J., Pompilus, M., Pinto, A.M., Grudny, M.M., Bruijnzeel, A.W., Merritt, M.E., 2024. Age-related differences in affective behaviors in mice: possible role of prefrontal cortical-hippocampal functional connectivity and metabolomic profiles. Front Aging Neurosci 16, 1356086.

Filippi, M., Basaia, S., Canu, E., Imperiale, F., Meani, A., Caso, F., Magnani, G., Falautano, M., Comi, G., Falini, A., Agosta, F., 2017. Brain network connectivity differs in early-onset neurodegenerative dementia. Neurology 89(17), 1764-1772.

Fuhrer, T.E., Palpagama, T.H., Waldvogel, H.J., Synek, B.J.L., Turner, C., Faull, R.L., Kwakowsky, A., 2017. Impaired expression of GABA transporters in the human Alzheimer's disease hippocampus, subiculum, entorhinal cortex and superior temporal gyrus. Neuroscience 351, 108-118.

Garcia-Marin, V., Blazquez-Llorca, L., Rodriguez, J.R., Boluda, S., Muntane, G., Ferrer, I., Defelipe, J., 2009. Diminished perisomatic GABAergic terminals on cortical neurons adjacent to amyloid plaques. Front Neuroanat 3, 28.

Garland, E.F., Dennett, O., Lau, L.C., Chatelet, D.S., Bottlaender, M., Nicoll, J.A.R., Boche, D., 2023. The mitochondrial protein TSPO in Alzheimer's disease: relation to the severity of AD pathology and the neuroinflammatory environment. J Neuroinflammation 20(1), 186.

Giorgio, J., Adams, J.N., Maass, A., Jagust, W.J., Breakspear, M., 2024. Amyloid induced hyperexcitability in default mode network drives medial temporal hyperactivity and early tau accumulation. Neuron 112(4), 676-686 e674.

Giulian, D., Li, J., Bartel, S., Broker, J., Li, X., Kirkpatrick, J.B., 1995. Cell surface morphology identifies microglia as a distinct class of mononuclear phagocyte. J Neurosci 15(11), 7712-7726.

Grandjean, J., Derungs, R., Kulic, L., Welt, T., Henkelman, M., Nitsch, R.M., Rudin, M., 2016. Complex interplay between brain function and structure during cerebral amyloidosis in APP transgenic mouse strains revealed by multi-parametric MRI comparison. Neuroimage 134, 1-11.

Grandjean, J., Schroeter, A., Batata, I., Rudin, M., 2014a. Optimization of anesthesia protocol for resting-state fMRI in mice based on differential effects of anesthetics on functional connectivity patterns. Neuroimage 102 Pt 2, 838-847.

Grandjean, J., Schroeter, A., He, P., Tanadini, M., Keist, R., Krstic, D., Konietzko, U., Klohs, J., Nitsch, R.M., Rudin, M., 2014b. Early alterations in functional connectivity and white matter structure in a transgenic mouse model of cerebral amyloidosis. J Neurosci 34(41), 13780-13789.

Guerreiro, R.J., Gustafson, D.R., Hardy, J., 2012. The genetic architecture of Alzheimer's disease: beyond APP, PSENs and APOE. Neurobiol Aging 33(3), 437-456.

Halder, S.K., Sasaki, K., Ueda, H., 2020. Ggamma7-specific prothymosin alpha deletion causes stress- and age-dependent motor dysfunction and anxiety. Biochem Biophys Res Commun 522(1), 264-269.

Hebb, A.L., Robertson, H.A., Denovan-Wright, E.M., 2004. Striatal phosphodiesterase mRNA and protein levels are reduced in Huntington's disease transgenic mice prior to the onset of motor symptoms. Neuroscience 123(4), 967-981.

Hedden, T., Van Dijk, K.R., Becker, J.A., Mehta, A., Sperling, R.A., Johnson, K.A., Buckner, R.L., 2009. Disruption of functional connectivity in clinically normal older adults harboring amyloid burden. J Neurosci 29(40), 12686-12694.

Hendriks, S., Peetoom, K., Bakker, C., van der Flier, W.M., Papma, J.M., Koopmans, R., Verhey, F.R.J., de Vugt, M., Kohler, S., Young-Onset Dementia Epidemiology Study, G., Withall, A., Parlevliet, J.L., Uysal-Bozkir, O., Gibson, R.C., Neita, S.M., Nielsen, T.R., Salem, L.C., Nyberg, J., Lopes, M.A., Dominguez, J.C., De Guzman, M.F., Egeberg, A., Radford, K., Broe, T., Subramaniam, M., Abdin, E., Bruni, A.C., Di Lorenzo, R., Smith, K., Flicker, L., Mol, M.O., Basta, M., Yu, D., Masika, G., Petersen, M.S., Ruano, L., 2021. Global Prevalence of Young-Onset Dementia: A Systematic Review and Meta-analysis. JAMA Neurol 78(9), 1080-1090.

Hirata-Fukae, C., Li, H.F., Hoe, H.S., Gray, A.J., Minami, S.S., Hamada, K., Niikura, T., Hua, F., Tsukagoshi-Nagai, H., Horikoshi-Sakuraba, Y., Mughal, M., Rebeck, G.W., LaFerla, F.M., Mattson, M.P., Iwata, N., Saido, T.C., Klein, W.L., Duff, K.E., Aisen, P.S., Matsuoka, Y., 2008. Females exhibit more extensive amyloid, but not tau, pathology in an Alzheimer transgenic model. Brain Res 1216, 92-103.

Hu, W., Pan, D., Wang, Y., Bao, W., Zuo, C., Guan, Y., Hua, F., Yang, M., Zhao, J., 2020. PET Imaging for Dynamically Monitoring Neuroinflammation in APP/PS1 Mouse Model Using [(18)F]DPA714. Front Neurosci 14, 810.

Hufgard, J.R., Williams, M.T., Vorhees, C.V., 2017. Phosphodiesterase-1b deletion confers depression-like behavioral resistance separate from stress-related effects in mice. Genes, brain, and behavior 16(8), 756-767.

Hyvarinen, A., 1999. Fast and robust fixed-point algorithms for independent component analysis. IEEE Trans Neural Netw 10(3), 626-634.

Ingala, S., Tomassen, J., Collij, L.E., Prent, N., van 't Ent, D., Ten Kate, M., Konijnenberg, E., Yaqub, M., Scheltens, P., de Geus, E.J.C., Teunissen, C.E., Tijms, B., Wink, A.M., Barkhof, F., van Berckel, B.N.M., Visser, P.J., den Braber, A., 2021. Amyloid-driven disruption of default mode network connectivity in cognitively healthy individuals. Brain Commun 3(4), fcab201.

Ishikawa, A., Nakamura, S., 2006. Ventral hippocampal neurons project axons simultaneously to the medial prefrontal cortex and amygdala in the rat. J Neurophysiol 96(4), 2134-2138.

Jankowsky, J.L., Fadale, D.J., Anderson, J., Xu, G.M., Gonzales, V., Jenkins, N.A., Copeland, N.G., Lee, M.K., Younkin, L.H., Wagner, S.L., Younkin, S.G., Borchelt, D.R., 2004. Mutant presenilins specifically elevate the levels of the 42 residue beta-amyloid peptide in vivo: evidence for augmentation of a 42-specific gamma secretase. Hum Mol Genet 13(2), 159-170.

Janus, C., Flores, A.Y., Xu, G., Borchelt, D.R., 2015. Behavioral abnormalities in APPSwe/PS1dE9 mouse model of AD-like pathology: comparative analysis across multiple behavioral domains. Neurobiol Aging 36(9), 2519-2532.

Jenkinson, M., Bannister, P., Brady, M., Smith, S., 2002. Improved optimization for the robust and accurate linear registration and motion correction of brain images. Neuroimage 17(2), 825-841.

Jonckers, E., Van Audekerke, J., De Visscher, G., Van der Linden, A., Verhoye, M., 2011. Functional connectivity fMRI of the rodent brain: comparison of functional connectivity networks in rat and mouse. PLoS One 6(4), e18876.

Kilgore, M., Miller, C.A., Fass, D.M., Hennig, K.M., Haggarty, S.J., Sweatt, J.D., Rumbaugh, G., 2010. Inhibitors of class 1 histone deacetylases reverse contextual memory deficits in a mouse model of Alzheimer's disease. Neuropsychopharmacology 35(4), 870-880.

Klein, A., Andersson, J., Ardekani, B.A., Ashburner, J., Avants, B., Chiang, M.C., Christensen, G.E., Collins, D.L., Gee, J., Hellier, P., Song, J.H., Jenkinson, M., Lepage, C., Rueckert, D., Thompson, P., Vercauteren, T., Woods, R.P., Mann, J.J., Parsey, R.V., 2009. Evaluation of 14 nonlinear deformation algorithms applied to human brain MRI registration. Neuroimage 46(3), 786-802.

Kotlarz, P., Nino, J.C., Febo, M., 2022. Connectomic analysis of Alzheimer's disease using percolation theory. Netw Neurosci 6(1), 213-233.

Kurucu, H., Colom-Cadena, M., Davies, C., Wilkins, L., King, D., Rose, J., Tzioras, M., Tulloch, J.H., Smith, C., Spires-Jones, T.L., 2022. Inhibitory synapse loss and accumulation of amyloid beta in inhibitory presynaptic terminals in Alzheimer's disease. Eur J Neurol 29(5), 1311-1323.

Lalonde, R., Kim, H.D., Maxwell, J.A., Fukuchi, K., 2005. Exploratory activity and spatial learning in 12-month-old APP(695)SWE/co+PS1/DeltaE9 mice with amyloid plaques. Neurosci Lett 390(2), 87-92.

Langfelder, P., Horvath, S., 2008. WGCNA: an R package for weighted correlation network analysis. BMC Bioinformatics 9, 559.

Langfelder, P., Horvath, S., 2012. Fast R Functions for Robust Correlations and Hierarchical Clustering. J Stat Softw 46(11).

Lauterborn, J.C., Scaduto, P., Cox, C.D., Schulmann, A., Lynch, G., Gall, C.M., Keene, C.D., Limon, A., 2021. Increased excitatory to inhibitory synaptic ratio in parietal cortex samples from individuals with Alzheimer's disease. Nat Commun 12(1), 2603.

Lawrence, M., Huber, W., Pages, H., Aboyoun, P., Carlson, M., Gentleman, R., Morgan, M.T., Carey, V.J., 2013. Software for computing and annotating genomic ranges. PLoS Comput Biol 9(8), e1003118.

Lee, J.Y., Cole, T.B., Palmiter, R.D., Suh, S.W., Koh, J.Y., 2002. Contribution by synaptic zinc to the gender-disparate plaque formation in human Swedish mutant APP transgenic mice. Proc Natl Acad Sci U S A 99(11), 7705-7710.

Li, Q.S., Sun, Y., Wang, T., 2020. Epigenome-wide association study of Alzheimer's disease replicates 22 differentially methylated positions and 30 differentially methylated regions. Clin Epigenetics 12(1), 149.

Lim, H.K., Nebes, R., Snitz, B., Cohen, A., Mathis, C., Price, J., Weissfeld, L., Klunk, W., Aizenstein, H.J., 2014. Regional amyloid burden and intrinsic connectivity networks in cognitively normal elderly subjects. Brain 137(Pt 12), 3327-3338.

Lituma, P.J., Woo, E., O'Hara, B.F., Castillo, P.E., Sibinga, N.E.S., Nandi, S., 2021. Altered synaptic connectivity and brain function in mice lacking microglial adapter protein Iba1. Proc Natl Acad Sci U S A 118(46).

Liu, D., Lu, H., Stein, E., Zhou, Z., Yang, Y., Mattson, M.P., 2018. Brain regional synchronous activity predicts tauopathy in 3xTgAD mice. Neurobiol Aging 70, 160-169.

Lorenzini, L., Ingala, S., Collij, L.E., Wottschel, V., Haller, S., Blennow, K., Frisoni, G., Chetelat, G., Payoux, P., Lage-Martinez, P., Ewers, M., Waldman, A., Wardlaw, J., Ritchie, C., Gispert, J.D., Mutsaerts, H., Visser, P.J., Scheltens, P., Tijms, B., Barkhof, F., Wink, A.M., 2023. Eigenvector centrality dynamics are related to Alzheimer's disease pathological changes in non-demented individuals. Brain Commun 5(3), fcad088.

Love, M.I., Huber, W., Anders, S., 2014. Moderated estimation of fold change and dispersion for RNA-seq data with DESeq2. Genome Biol 15(12), 550.

Ma, Y., Reyes-Dumeyer, D., Piriz, A., Recio, P., Mejia, D.R., Medrano, M., Lantigua, R.A., Vonsattel, J.P.G., Tosto, G., Teich, A.F., Ciener, B., Leskinen, S., Sivakumar, S., DeTure, M., Ranjan, D., Dickson, D., Murray, M., Lee, E., Wolk, D.A., Jin, L.W., Dugger, B.N., Hiniker, A., Rissman, R.A., Mayeux, R., Vardarajan, B.N., 2024. Multi-omics Characterization of Epigenetic and Genetic Risk of Alzheimer Disease in Autopsied Brains from two Ethnic Groups. medRxiv.

McFarland, K.N., Ceballos, C., Rosario, A., Ladd, T., Moore, B., Golde, G., Wang, X., Allen, M., Ertekin-Taner, N., Funk, C.C., Robinson, M., Baloni, P., Rappaport, N., Chakrabarty, P., Golde, T.E., 2021. Microglia show differential transcriptomic response to Abeta peptide aggregates ex vivo and in vivo. Life Sci Alliance 4(7).

Mitew, S., Kirkcaldie, M.T., Dickson, T.C., Vickers, J.C., 2013. Altered synapses and gliotransmission in Alzheimer's disease and AD model mice. Neurobiol Aging 34(10), 2341-2351.

Morgan, M., Pages, H., Obenchain, V., Hayden, N., 2023. Rsamtools: Binary alignment (BAM), FASTA, variant call (BCF), and tabix file import. R package version 2.18.0, https://bioconductor.org/packages/Rsamtools.

Newman, M.E., 2002. Assortative mixing in networks. Physical review letters 89(20), 208701.

Niraula, S., Yan, S.S., Subramanian, J., 2024. Amyloid Pathology Impairs Experience-Dependent Inhibitory Synaptic Plasticity. J Neurosci 44(5).

Orsini, C.A., Kim, J.H., Knapska, E., Maren, S., 2011. Hippocampal and prefrontal projections to the basal amygdala mediate contextual regulation of fear after extinction. J Neurosci 31(47), 17269-17277.

Ouimet, C.C., Greengard, P., 1990. Distribution of DARPP-32 in the basal ganglia: an electron microscopic study. J Neurocytol 19(1), 39-52.

Parent, M.J., Zimmer, E.R., Shin, M., Kang, M.S., Fonov, V.S., Mathieu, A., Aliaga, A., Kostikov, A., Do Carmo, S., Dea, D., Poirier, J., Soucy, J.P., Gauthier, S., Cuello, A.C., Rosa-Neto, P., 2017. Multimodal Imaging in Rat Model Recapitulates Alzheimer's Disease Biomarkers Abnormalities. J Neurosci 37(50), 12263-12271.

Petrache, A.L., Rajulawalla, A., Shi, A., Wetzel, A., Saito, T., Saido, T.C., Harvey, K., Ali, A.B., 2019. Aberrant Excitatory-Inhibitory Synaptic Mechanisms in Entorhinal Cortex Microcircuits During the Pathogenesis of Alzheimer's Disease. Cereb Cortex 29(4), 1834-1850.

Pini, L., Geroldi, C., Galluzzi, S., Baruzzi, R., Bertocchi, M., Chito, E., Orini, S., Romano, M., Cotelli, M., Rosini, S., Magnaldi, S., Morassi, M., Cobelli, M., Bonvicini, C., Archetti, S., Zanetti, O., Frisoni, G.B., Pievani, M., 2020. Age at onset reveals different functional connectivity abnormalities in prodromal Alzheimer's disease. Brain Imaging Behav 14(6), 2594-2605.

Pompilus, M., Colon-Perez, L.M., Grudny, M.M., Febo, M., 2020. Contextual experience modifies functional connectome indices of topological strength and efficiency. Sci Rep 10(1), 19843.

Qiu, T., Luo, X., Shen, Z., Huang, P., Xu, X., Zhou, J., Zhang, M., Alzheimer's Disease Neuroimaging, I., 2016. Disrupted Brain Network in Progressive Mild Cognitive Impairment Measured by Eigenvector Centrality Mapping is Linked to Cognition and Cerebrospinal Fluid Biomarkers. J Alzheimers Dis 54(4), 1483-1493.

Reed, T.M., Repaske, D.R., Snyder, G.L., Greengard, P., Vorhees, C.V., 2002. Phosphodiesterase 1B knock-out mice exhibit exaggerated locomotor hyperactivity and DARPP-32 phosphorylation in response to dopamine agonists and display impaired spatial learning. J Neurosci 22(12), 5188-5197.

Rubinov, M., Sporns, O., 2010. Complex network measures of brain connectivity: uses and interpretations. Neuroimage 52(3), 1059-1069.

Sadaka, A.H., Canuel, J., Febo, M., Johnson, C.T., Bradshaw, H.B., Ortiz, R., Ciumo, F., Kulkarni, P., Gitcho, M.A., Ferris, C.F., 2023. Effects of inhaled cannabis high in Delta9-THC or CBD on the aging brain: A translational MRI and behavioral study. Front Aging Neurosci 15, 1055433.

Sakthivel, R., Criado-Marrero, M., Barroso, D., Braga, I.M., Bolen, M., Rubinovich, U., Hery, G.P., Grudny, M.M., Koren, J., 3rd, Prokop, S., Febo, M., Abisambra, J.F., 2023. Fixed Time-Point Analysis Reveals Repetitive Mild Traumatic Brain Injury Effects on Resting State Functional Magnetic Resonance Imaging Connectivity and Neuro-Spatial Protein Profiles. J Neurotrauma.

Sforazzini, F., Schwarz, A.J., Galbusera, A., Bifone, A., Gozzi, A., 2014. Distributed BOLD and CBV-weighted resting-state networks in the mouse brain. Neuroimage 87, 403-415.

Shah, D., Deleye, S., Verhoye, M., Staelens, S., Van der Linden, A., 2016. Resting-state functional MRI and [18F]-FDG PET demonstrate differences in neuronal activity between commonly used mouse strains. Neuroimage 125, 571-577.

Shah, D., Jonckers, E., Praet, J., Vanhoutte, G., Delgado, Y.P.R., Bigot, C., D'Souza, D.V., Verhoye, M., Van der Linden, A., 2013. Resting state FMRI reveals diminished functional connectivity in a mouse model of amyloidosis. PLoS One 8(12), e84241.

Skouras, S., Falcon, C., Tucholka, A., Rami, L., Sanchez-Valle, R., Llado, A., Gispert, J.D., Molinuevo, J.L., 2019. Mechanisms of functional compensation, delineated by eigenvector centrality mapping, across the pathophysiological continuum of Alzheimer's disease. Neuroimage Clin 22, 101777.

Stone, D.J., Walsh, J., Benes, F.M., 1999. Localization of cells preferentially expressing GAD(67) with negligible GAD(65) transcripts in the rat hippocampus. A double in situ hybridization study. Brain research. Molecular brain research 71(2), 201-209.

Stroppolo, A., Tian, C., Guinea, B., Olm, V., Sheffield, R., Sommer, J., Ehrlich, M.E., 2004. 17beta-Estradiol promotes striatal medium size spiny neuronal maturation in vitro. Neuroendocrinology 79(5), 259-267.

Surala, M., Soso-Zdravkovic, L., Munro, D., Rifat, A., Ouk, K., Vida, I., Priller, J., Madry, C., 2024. Lifelong absence of microglia alters hippocampal glutamatergic networks but not synapse and spine density. EMBO Rep.

Swanson, L.W., Kohler, C., 1986. Anatomical evidence for direct projections from the entorhinal area to the entire cortical mantle in the rat. J Neurosci 6(10), 3010-3023.

Teague, C.D., Markovic, T., Zhou, X., Martinez-Rivera, F.J., Minier-Toribio, A., Zinsmaier, A., Pulido, N.V., Schmidt, K.H., Lucerne, K.E., Godino, A., van der Zee, Y.Y., Ramakrishnan, A., Futamura, R., Browne, C.J., Holt, L.M., Yim, Y.Y., Azizian, C.H., Walker, D.M., Shen, L., Dong, Y., Zhang, B., Nestler, E.J., 2024. Circuit-wide gene network analysis reveals sex-specific roles for phosphodiesterase 1b in cocaine addiction. J Neurosci.

Thierry, A.M., Gioanni, Y., Degenetais, E., Glowinski, J., 2000. Hippocampo-prefrontal cortex pathway: anatomical and electrophysiological characteristics. Hippocampus 10(4), 411-419.

Tremblay, M.E., Lowery, R.L., Majewska, A.K., 2010. Microglial interactions with synapses are modulated by visual experience. PLoS Biol 8(11), e1000527.

Tremblay, M.E., Majewska, A.K., 2011. A role for microglia in synaptic plasticity? Commun Integr Biol 4(2), 220-222.

Verret, L., Mann, E.O., Hang, G.B., Barth, A.M., Cobos, I., Ho, K., Devidze, N., Masliah, E., Kreitzer, A.C., Mody, I., Mucke, L., Palop, J.J., 2012. Inhibitory interneuron deficit links altered network activity and cognitive dysfunction in Alzheimer model. Cell 149(3), 708-721.

Wake, H., Moorhouse, A.J., Jinno, S., Kohsaka, S., Nabekura, J., 2009. Resting microglia directly monitor the functional state of synapses in vivo and determine the fate of ischemic terminals. J Neurosci 29(13), 3974-3980.

Wang, J., Tanila, H., Puolivali, J., Kadish, I., van Groen, T., 2003. Gender differences in the amount and deposition of amyloidbeta in APPswe and PS1 double transgenic mice. Neurobiol Dis 14(3), 318-327.

Wang, Q., Ding, S.L., Li, Y., Royall, J., Feng, D., Lesnar, P., Graddis, N., Naeemi, M., Facer, B., Ho, A., Dolbeare, T., Blanchard, B., Dee, N., Wakeman, W., Hirokawa, K.E., Szafer, A., Sunkin, S.M., Oh, S.W., Bernard, A., Phillips, J.W., Hawrylycz, M., Koch, C., Zeng, H., Harris, J.A., Ng, L., 2020. The Allen Mouse Brain Common Coordinate Framework: A 3D Reference Atlas. Cell 181(4), 936-953 e920.

Wang, Y., Ghumare, E., Vandenberghe, R., Dupont, P., 2017. Comparison of Different Generalizations of Clustering Coefficient and Local Efficiency for Weighted Undirected Graphs. Neural computation 29(2), 313-331.

Weiner, J., Sun, W.L., Zhou, L., Kreiter, C.M., Jenab, S., Quinones-Jenab, V., 2009. PKA-mediated responses in females' estrous cycle affect cocaine-induced responses in dopamine-mediated intracellular cascades. Neuroscience 161(3), 865-876.

Whitesell, J.D., Buckley, A.R., Knox, J.E., Kuan, L., Graddis, N., Pelos, A., Mukora, A., Wakeman, W., Bohn, P., Ho, A., Hirokawa, K.E., Harris, J.A., 2019. Whole brain imaging reveals distinct spatial patterns of amyloid beta deposition in three mouse models of Alzheimer's disease. J Comp Neurol 527(13), 2122-2145.

Wu, J., Fu, B., Lei, H., Tang, H., Wang, Y., 2016. Gender differences of peripheral plasma and liver metabolic profiling in APP/PS1 transgenic AD mice. Neuroscience 332, 160-169.

Xia, M., Wang, J., He, Y., 2013. BrainNet Viewer: a network visualization tool for human brain connectomics. PLoS One 8(7), e68910.

Yang, Z., Zhu, T., Pompilus, M., Fu, Y., Zhu, J., Arjona, K., Arja, R.D., Grudny, M.M., Plant, H.D., Bose, P., Wang, K.K., Febo, M., 2021. Compensatory functional connectome changes in a rat model of traumatic brain injury. Brain Commun 3(4), fcab244.

Yushkevich, P.A., Piven, J., Hazlett, H.C., Smith, R.G., Ho, S., Gee, J.C., Gerig, G., 2006. User-guided 3D active contour segmentation of anatomical structures: significantly improved efficiency and reliability. Neuroimage 31(3), 1116-1128.

Zhan, Y., Paolicelli, R.C., Sforazzini, F., Weinhard, L., Bolasco, G., Pagani, F., Vyssotski, A.L., Bifone, A., Gozzi, A., Ragozzino, D., Gross, C.T., 2014. Deficient neuron-microglia signaling results in impaired functional brain connectivity and social behavior. Nat Neurosci 17(3), 400-406.

Zhang, X., Zeng, Q., Wang, Y., Jin, Y., Qiu, T., Li, K., Luo, X., Wang, S., Xu, X., Liu, X., Zhao, S., Li, Z., Hong, L., Li, J., Zhong, S., Zhang, T., Huang, P., Zhang, B., Zhang, M., Chen, Y., 2024. Alteration of functional connectivity network in population of objectively-defined subtle cognitive decline. Brain Commun 6(1), fcae033.

Zhang, Y., Chen, K., Sloan, S.A., Bennett, M.L., Scholze, A.R., O'Keeffe, S., Phatnani, H.P., Guarnieri, P., Caneda, C., Ruderisch, N., Deng, S., Liddelow, S.A., Zhang, C., Daneman, R., Maniatis, T., Barres, B.A., Wu, J.Q., 2014. An RNA-sequencing transcriptome and splicing database of glia, neurons, and vascular cells of the cerebral cortex. J Neurosci 34(36), 11929-11947.

Zheng, H., Xu, H., Uljon, S.N., Gross, R., Hardy, K., Gaynor, J., Lafrancois, J., Simpkins, J., Refolo, L.M., Petanceska, S., Wang, R., Duff, K., 2002. Modulation of A(beta) peptides by estrogen in mouse models. J Neurochem 80(1), 191-196.

Zhou, J., Li, K., Luo, X., Zeng, Q., Jiaerken, Y., Wang, S., Xu, X., Liu, X., Li, Z., Zhang, T., Fu, Y., Zhao, S., Huang, P., Zhang, M., 2021. Distinct impaired patterns of intrinsic functional network centrality in patients with early- and late-onset Alzheimer's disease. Brain Imaging Behav 15(5), 2661-2670.

Zhou, L., Nazarian, A., Sun, W.L., Jenab, S., Quinones-Jenab, V., 2009. Basal and cocaine-induced sex differences in the DARPP-32-mediated signaling pathway. Psychopharmacology (Berl) 203(1), 175-183.

Zuo, X.N., Ehmke, R., Mennes, M., Imperati, D., Castellanos, F.X., Sporns, O., Milham, M.P., 2012. Network centrality in the human functional connectome. Cereb Cortex 22(8), 1862-1875.

Supplementary figures and legends

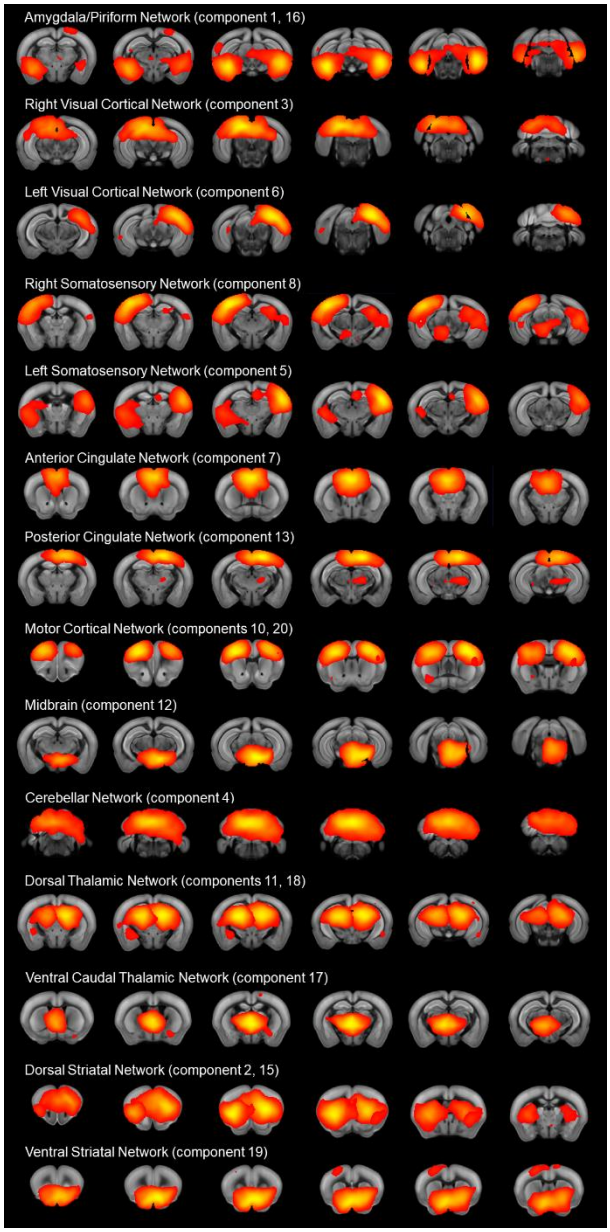

Supplementary Figure 1. Independent component analysis of 28 mouse fMRI scans yielded 20 distinct networks. Networks were identified based on prior studies and on location of peak z statistic voxels (higher intensity/higher functional connectivity voxels highlighted in yellow and lower intensity in orange hue). Assigned network names are above each row of ICA maps, with component numbers in parenthesis. ICA maps are organized rostral to caudal from left to right. Z statistical maps are thresholded using threshold free cluster enhanced approach and are overlaid on to the Allen Mouse Brain Common Coordinate Reference atlas (CCFv3).

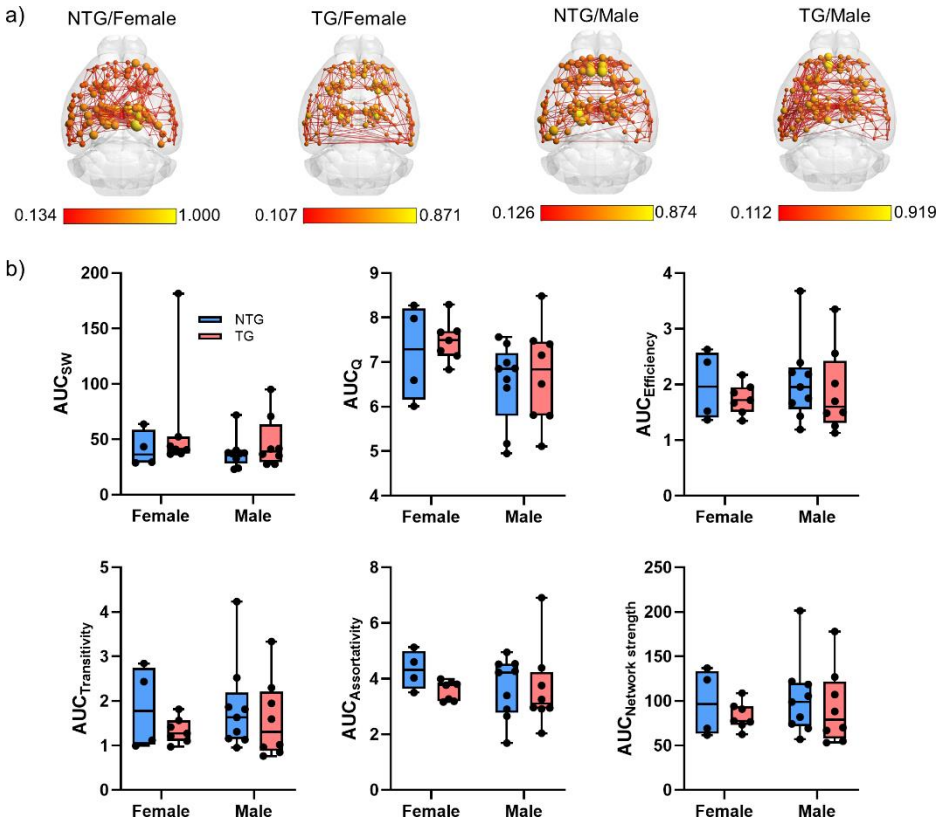

Supplementary Figure 2. No significant differences in globally estimated graph theory measures. a) Functional connectome maps averaged within groups and illustrate node strength and edge strength (Pearson correlations) as spherical nodes and lines connecting nodes. Node strength is reflected in sphere size and color intensity (scale bar below maps indicate Fisher z-transformed r values rescaled between 0 and 1). Edges are thresholded at 6% density for visual purposes. b) Comparison of several network measures (converted to area under the curve for network densities between 2-40%) between male and female NTG and TG mice.

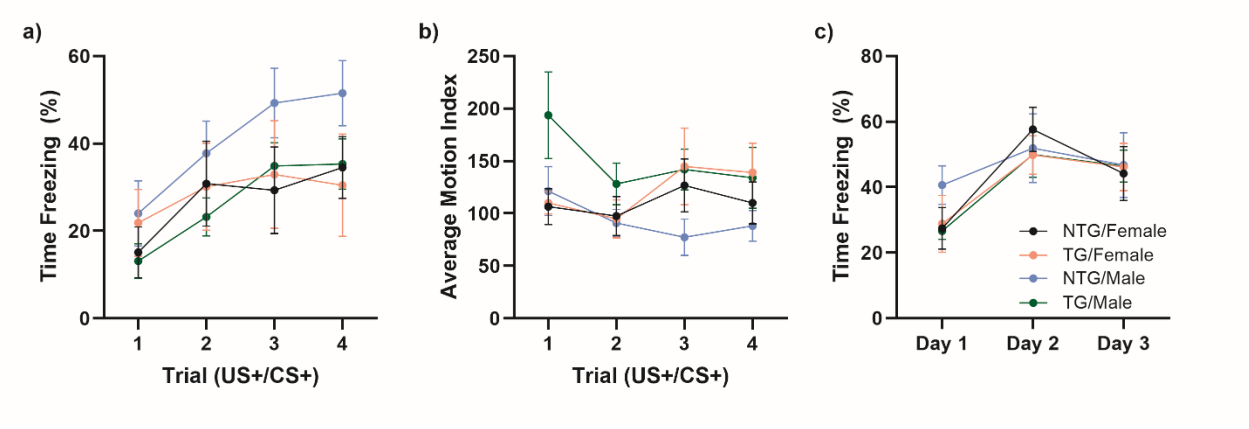

Supplementary Figure 3. No significant differences between NTG and TG mice in fear conditioning tests. a) Percent freezing responses per 60 second trials on day one of conditioned stimulus auditory cue/context (conditioned stimulus, CS) pairing with a foot shock (unconditioned stimulus, US). b) Motor activity averaged over each conditioning trial on day 1. c) Percent freezing responses averaged over 60 min trial epochs per day. Day 1 represents fear learning, day 2 recall, and day 3 recall in a modified context (on days 2 and 3 auditory cue presented in the absence of shock). Data in plots are presented as mean ± standard error.

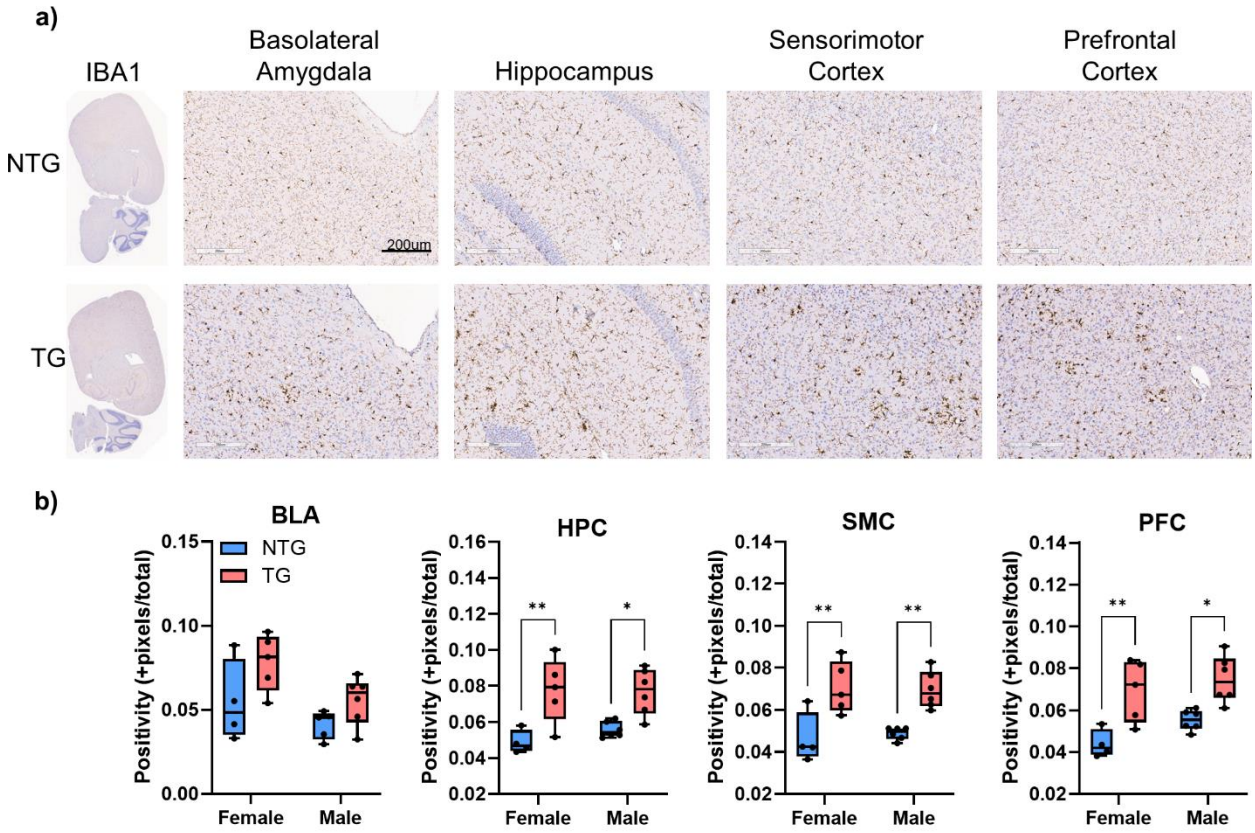

Supplementary Figure 4. Amyloidosis is associate with an increase microglial abundance in both male and female mice. a) Representative histological Iba1 antibody-stained sections from NTG and TG mouse basolateral amygdala (BLA), prefrontal cortex (PFC), somatomotor cortex (SMC), and hippocampus (HPC). b) Comparison of microglial abundance between male (M) and female (F) NTG and TG mice. Data in a-b are box-whisker showing median, minimum-maximum values and individual data points. Asterisks are *p < 0.05, **p < 0.01.